



### 저작자표시-비영리-동일조건변경허락 2.0 대한민국

이용자는 아래의 조건을 따르는 경우에 한하여 자유롭게

- 이 저작물을 복제, 배포, 전송, 전시, 공연 및 방송할 수 있습니다.
- 이차적 저작물을 작성할 수 있습니다.

다음과 같은 조건을 따라야 합니다:



저작자표시. 귀하는 원저작자를 표시하여야 합니다.



비영리. 귀하는 이 저작물을 영리 목적으로 이용할 수 없습니다.



동일조건변경허락. 귀하가 이 저작물을 개작, 변형 또는 가공했을 경우에는, 이 저작물과 동일한 이용허락조건하에서만 배포할 수 있습니다.

- 귀하는, 이 저작물의 재이용이나 배포의 경우, 이 저작물에 적용된 이용허락조건을 명확하게 나타내어야 합니다.
- 저작권자로부터 별도의 허가를 받으면 이러한 조건들은 적용되지 않습니다.

저작권법에 따른 이용자의 권리는 위의 내용에 의하여 영향을 받지 않습니다.

이것은 [이용허락규약\(Legal Code\)](#)을 이해하기 쉽게 요약한 것입니다.

[Disclaimer](#)

Electrospun nanofibers of manganese oxides with  
mixed phase for supercapacitor



Department of Energy Engineering  
Graduate School of UNIST

2014

# Electrospun nanofibers of manganese oxides with mixed phase for supercapacitor

A thesis  
submitted to the Graduate School of UNIST  
in partial fulfillment of the  
requirements for the degree of  
Master of Science

Eun-Hee Lee

02. 20. 2014

Approved by



Major Advisor

Byeong-Su Kim

# Electrospun nanofibers of manganese oxides with mixed phase for supercapacitor

Eun-Hee Lee

This certifies that the thesis of Eun-Hee Lee is approved.

02. 20. 2014

Signature



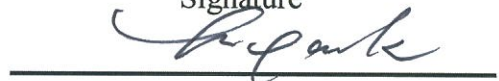
Thesis supervisor: Byeong-Su Kim

Signature



Soojin Park

Signature



Jongnam Park

# Contents

Abstract.....	1
List of Figures.....	2
List of Tables.....	4
I. Introduction.....	5
1.1 Supercapacitor.....	5
1.1.1 Principle of supercapacitor.....	8
1.1.2 Manganese oxide as active material of supercapacitor.....	11
1.1.3 Effect of electrode structure.....	13
1.2 Electrospinning .....	14
1.2.1 Parameter of electrospinning.....	18
1.2.2 Control of structure of electrospun NFs.....	18
1.2.3 Preparation of electrospun inorganic NFs.....	21
1.2.4 Electrospun fibers for supercapacitor.....	21
II. Experiments.....	23
2.1 Preparation of electrospun MnO <sub>x</sub> NFs.....	23
2.2 Electrochemical measurements.....	23
2.3 Characterizations.....	23
III. Results and Discussion.....	25
3.1 Characterization of electrospun MnO <sub>x</sub> NFs.....	25
3.2 Electrochemical performance of electrospun MnO <sub>x</sub> NFs.....	26
IV. Conclusion.....	34
V. Reference.....	35

## Abstract

Electrospinning technique produces continuous fibers of various structures and composition with diameters ranging from a few micrometers to nanometers. Particularly, the three-dimensional (3D) non-woven fiber matrix contains a large porous network structure which is highly suitable for electrode applications that can facilitate the access of electrolytes into the active species. For that, we have fabricated the inorganic manganese oxide ( $\text{MnO}_x$ ) nanofibers (NFs) of varying composition by electrospinning technique for supercapacitor applications.  $\text{MnO}_x$  is promising for pseudocapacitor due to their fine specific capacitance, low cost, and environmental benignity. In this study, we prepared the electrospun NFs of  $\text{Mn}(\text{OAc})_2/\text{poly}(\text{vinyl pyrrolidone})$  (PVP) composite by using electrospinning technique. The as-prepared inorganic NFs were annealed at different temperatures to remove the polymer matrix and resulted in the  $\text{MnO}_x$  NFs of varying composition. Interestingly, we found that the capacitance of  $\text{MnO}_x$  NFs annealed at 500 °C is highest among all samples with contained a mixed phase of  $\text{Mn}_2\text{O}_3$  and  $\text{Mn}_3\text{O}_4$ .

## List of Figures

**Figure 1.** A simplified Ragone plot of specific energy versus specific power for the various electrochemical energy storage devices.

**Figure 2.** Schematic of two different energy storage mechanisms via (A) electrochemical double layer capacitances (EDLCs) or (B) redox reactions based pseudocapacitance.

**Figure 3.** The capacitance performance for both carbon based EDLC electrodes and pseudocapacitor electrodes (including transition metal oxides and conducting polymers.) Reproduced with permission. copyright 2008, the electrochemical society.

**Figure 4.** Polyhedral representation of the eight Mn oxides reported : (a)  $\beta$ -MnO<sub>2</sub>, (b) R-MnO<sub>2</sub>, (c)  $\alpha$ -MnO<sub>2</sub>, (d)  $\delta$ -MnO<sub>2</sub>, (e)  $\lambda$ -MnO<sub>2</sub>, (f) LiMn<sub>2</sub>O<sub>4</sub>, (g) Mn<sub>2</sub>O<sub>3</sub>, and (h) Mn<sub>3</sub>O<sub>4</sub>. The light, dark, and black polyhedral represent Mn<sup>2+</sup> tetrahedral, Mn<sup>3+</sup> and Mn<sup>4+</sup> octahedral, and Li<sup>1+</sup> tetrahedral, respectively. And black spheres represent K<sup>+</sup> ions.

**Figure 5.** Schematic illustration of the electrospinning technique.

**Figure 6.** Photographs illustrating the instability region of a liquid jet electrospun from an aqueous solution of poly(ethylene oxide) (PEO).

**Figure 7.** Relative proportion of publications in main areas of applications of electrospinning in the period of 2000–2010

**Figure 8.** Number of research articles concerning electrospun nanofiber applications in energy devices published in the period of 2001–2010 (keywords electrospinning + fuel cells, electrospinning + Li-ion batteries, electrospinning + solar cells, electrospinning + supercapacitors).

**Figure 9.** (A) Schematic illustration of the setup used to prepare the hollow NFs by electrospinning. It concerns the use of a spinneret composed of two coaxial capillaries, through which mineral oil and an ethanol solution including titanium tetraisopropoxide and PVP were concurrently ejected to form a compound jet. (B) TEM image of the as-spun hollow NFs whose walls were made of a composite of amorphous TiO<sub>2</sub> and PVP. (C) TEM image of anatase hollow NFs that were obtained by annealing the composite nanotube at 500 °C in air.

**Figure 10.** SEM micrographs of PVP/PLA 1:1 fibers : (a) residual PLLA fiber after selective removal of PVP, (b) residual PDLLA fiber after selective removal of PVP. Copyright Polymer Engineering and science

**Figure 11.** Schematic illustration for the fabrication of the electrospun NFs and subsequent calcination process for hybrid  $\text{MnO}_x$  NFs supercapacitors.

**Figure 12.** TGA curves of (a) pure electrospun PVP NFs prepared with PVP powder ( $M_w$  1,300,000 g/mol) in deionized water (20 wt%), (b)  $\text{Mn}(\text{OAc})_2$  powder and (c, d) electrospun  $\text{Mn}(\text{OAc})_2/\text{PVP}$  NFs which were made by dissolving a manganese acetate (20 wt%) in PVP solution (20 wt%). TGA plots were measured in (a - c) air and (d)  $\text{N}_2$  atmosphere at a heating rate of 5 °C/min.

**Figure 13.** (a) SEM images of as-spun  $\text{Mn}(\text{OAc})_2/\text{PVP}$  NFs. (b-e) SEM images of  $\text{MnO}_x$  NFs produced from the  $\text{Mn}(\text{OAc})_2/\text{PVP}$  NFs by calcining at (b) 400, (c) 500, (d) 600, and (e) 700 °C for 2 h in air. The inset graphs show the diameter distribution of each NFs. (f) Plot of average diameter obtained from more than 50 individual SEM images as a function of the calcination temperature. The standard deviations are given as error bar.

**Figure 14.** (a) XRD patterns of the  $\text{MnO}_x$  NFs after calcining at 400-700 °C compared to the patterns of neat  $\text{Mn}_3\text{O}_4$  and  $\text{Mn}_2\text{O}_3$ . (b) Plot of relative phase compositions of  $\text{MnO}_x$  NFs as a function of the calcination temperature. (c) Schematic representation of the phase changes of  $\text{MnO}_x$  NFs as a function of the temperature.

**Figure 15.** (a) TEM image, and (b) electron diffraction pattern of  $\text{MnO}_x$  NFs calcined at 500 °C, (c) EDS mapping of Mn and O in  $\text{MnO}_x$  NF calcined at 500 °C.

**Figure 16.** (a) Cyclic voltammetry (CV) curves at a scan rate of 200 mV/s of all  $\text{MnO}_x$  NFs calcined at the specified temperatures. (b) A plot of the current densities of the  $\text{MnO}_x$  NFs calcined at 500 °C at scan rates from 5 to 200 mV/s. (c) Dependence of the capacitance on the calcination temperature. (d) Galvanostatic charge-discharge curves of  $\text{MnO}_x$  NFs calcined at the specified temperatures at a current density of 1 A/g. (e)  $C_{sp,CV}$  and  $C_{sp,G}$  of electrodes prepared from  $\text{MnO}_x$  as a function of the calcination temperature. (f) Nyquist plots of the electrochemical impedance spectroscopy (EIS) for the electrospun  $\text{MnO}_x$  electrodes as a function of the calcination temperature.

**Figure 17.** The equivalent circuit from the electrochemical impedance spectroscopy (EIS) analysis.



## List of Tables

**Table 1.** Comparison of typical capacitor and battery characteristics.

**Table 2.** EIS data of  $\text{MnO}_x$  NFs prepared at different calcination temperatures.

## I. INTRODUCTION

In recent years, problems of fossil fuel exhaustion and environmental pollution is becoming a major issue in the world. To resolve these problems, interest in eco-friendly energy source is increasing.<sup>1-3</sup> Furthermore, developments of new energy source and conversion system with high efficiency, low cost, and environmental benignity were required due to increase of demands of portable electronics and electrical vehicles.<sup>4-7</sup> Especially energy storage and conversion system, including rechargeable battery, fuel cell, supercapacitor have been studied to replace fossil fuels. Among electrochemical devices, supercapacitors which exhibit relatively high power density, fast charging/discharging rate, and good cycle stability are attractive that can substitute for batteries.<sup>8-12</sup> Due to its low energy density in comparison with batteries, studies for improving the supercapacitor performance are also currently being performed.

### 1.1 Supercapacitor

Among various energy storage systems, electrochemical energy storage system, such as fuel cells, batteries and capacitors, is very attractive devices.<sup>13-14</sup> There is the common feature of these devices that energy generating processes occur at boundary between the electrode and the electrolyte. Recently, the demand of future systems including portable electronics and electrical vehicles gradually is increasing.<sup>8</sup> Therefore, the performance of electrochemical energy storage systems has to be developed in order to meet the requirements.

**Figure 1** shows the Ragone plot which indicates specific power and specific energy of electrochemical energy storage devices for the most important energy storage devices. There are two key parameters to evaluate the performance of energy storage devices.<sup>15-17</sup> One is energy density ( $E$ ) which means the amount of energy stored in a given system or region of space per unit volume or mass and it can be described by the following equation (1) :

$$E = \frac{1}{2} CV^2 \quad (1)$$

where,  $C$  and  $V$  mean the specific capacitance and the voltage, respectively. The other factor is power density ( $P$ ) which is the amount of power (time rate of energy transfer) per unit volume and it can be described by the following equation (2) :

$$P_{max} = \frac{1}{4R_s} V_i^2 \quad (2)$$

where,  $R_s$  and  $V_i$  mean the equivalent series resistance (ESR) and the initial voltage, respectively. As shown the Ragone plot, batteries and fuel cells are regarded as high energy devices, while these devices have the low power density.<sup>18-20</sup> In contrast with fuel cells and batteries, the general capacitors are regarded as high power devices, but it can't produce a high energy density to meet requirement for long-term duration.<sup>8, 16</sup>

There exist the basic differences of batteries and capacitors depending on the charge storage

mechanisms and materials. In case of batteries, storing charge occurs in bulk electrode through faradaic reactions. Batteries consist of a negative and positive electrode material, an electrolyte that allows ions to transfer between the electrodes, and terminals that allow current to flow out of the battery to perform work.<sup>7, 21-22</sup>

Supercapacitors can offer the ability storing the energy within a few seconds compared with long charge/discharge time (tens of minutes or more time) of batteries. Furthermore, supercapacitors demonstrate excellent cycle life (commonly measured in hundreds of thousands to millions of cycles) which is around three times higher than that of batteries.<sup>5, 9-10</sup> Also, supercapacitors provide high reliability compared to batteries, leading to a lower maintenance cost (**Table 1**).<sup>23</sup> As a result, supercapacitors have been used in various fields ranging from portable electronics to large industrial power management. In the past decade, supercapacitor technology has developed greatly leading to enhance performance due to the development of new electrode materials such as nanomaterials and hybrid systems.

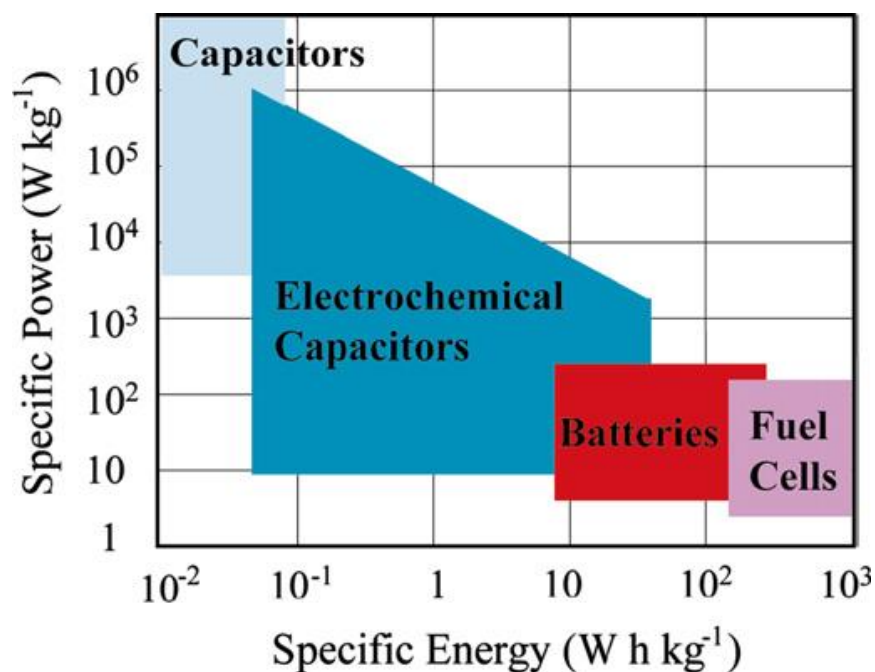


**Figure 1.** A simplified Ragone plot of specific energy versus specific power for the various electrochemical energy storage devices.<sup>15</sup>

Characteristic	Electrolytic capacitor	Carbon supercapacitor	Battery
Specific energy (Wh/kg)	<0.1	1-10	10-100
Specific power (W/kg)	$\gg 10000$	500-10000	<1000
Discharge time	$10^{-6}$ to $10^{-3}$ s	S to min	0.3-3h
Charging time	$10^{-6}$ to $10^{-3}$ s	S to min	1-5h
Charge/discharge efficiency (%)	$\sim 100$	85-98	70-85
Cycle-life (cycles)	Infinite	>500000	$\sim 1000$
Charge stored determinates	Electrode area and dielectric	Electrode microstructure and electrolyte	Active mass and thermodynamics

**Table 1.** Comparison of typical capacitor and battery characteristics.<sup>23</sup>

### 1.1.1 Principle of capacitors

Supercapacitor is divided into two types depending on the charge storage mechanism and active electrode materials. One is electrochemical double-layer capacitors (EDLCs) and the other is pseudocapacitors.<sup>6</sup> The EDLCs store the charges through reversible ion absorption on interface between the electrode and electrolyte and typically use carbon based materials with high surface area as active materials (**Figure 2 a**).<sup>24-27</sup> EDLCs can offer very high power density and good cycling stability owing to their fast electrochemical process. In case of EDLCs, the specific capacitance depends on the electrode materials such as carbon based nanomaterials and the electrolytes need to be carefully chosen to maximize the operating voltage.<sup>8, 15</sup> For instance, specific capacitance of EDLCs with aqueous acid or alkaline electrolytes is commonly higher than organic electrolytes.<sup>16</sup> Furthermore, it allows very fast energy density and higher power performance. But despite their advantages, it is not enough to alternate the conventional batteries because of its a relatively low energy density.

In contrast to EDLCs, the pseudocapacitors store charges through the fast and reversible electron exchange reactions (chemical redox reactions, faradaic reactions) on the electrode surface (**Figure 2 b**).<sup>24, 28-30</sup> The pseudocapacitors can increase specific capacitance and energy density than EDLCs (**Figure 3**).<sup>31-32</sup> However, it has the problems which are cost and low stability during cycling due to the fast redox reaction. Generally, transition metal oxides and electronically conducting polymers were used for the pseudocapacitive materials. The transition metal oxides include ruthenium oxide ( $\text{RuO}_2$ ),<sup>33-34</sup> manganese oxide ( $\text{MnO}_x$ ),<sup>35-36</sup> nickel oxide ( $\text{NiO}$ ),<sup>37-38</sup> iron oxide ( $\text{Fe}_3\text{O}_4$ )<sup>39</sup> and others. On the other hand, the typical conducting polymers are polyanilines, polypyrroles, and other  $\pi$ -conjugated polymers.<sup>40-41</sup> The specific capacitance of pseudocapacitive materials is higher than that of carbon based materials which are active materials of EDLCs. Among of pseudocapacitive materials,  $\text{RuO}_2$  is a widely studied active material owing to its high theoretical specific capacitance (1358 F/g) and good electrical conductivity ( $3 \times 10^2$  S/cm). Although  $\text{RuO}_2$  can demonstrate excellent electrochemical performance, it has cost problem because it is rare. Therefore, considerable efforts to replace  $\text{RuO}_2$  have been tried to develop inexpensive transition metal oxide including  $\text{MnO}_x$ ,  $\text{NiO}$ , and  $\text{Fe}_3\text{O}_4$ . Among many transition metal oxides,  $\text{MnO}_x$  is clearly noteworthy, displaying a fine specific capacitance (200-600 F/g) and reversible charge discharge feature with its natural abundance and low cost.<sup>35-36, 42-44</sup>

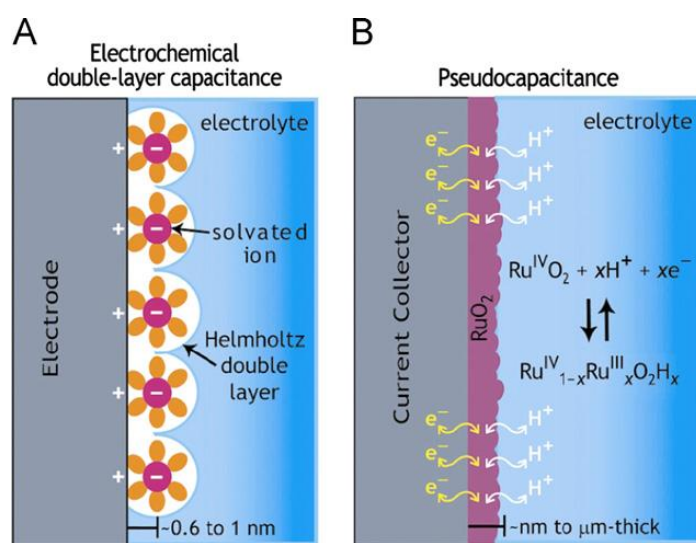


**Figure 2.** Schematic of two different energy storage mechanisms via (A) electrochemical double layer capacitances (EDLCs) or (B) redox reactions based pseudocapacitance.<sup>24</sup> Copyright 2011, Materials Research Society.

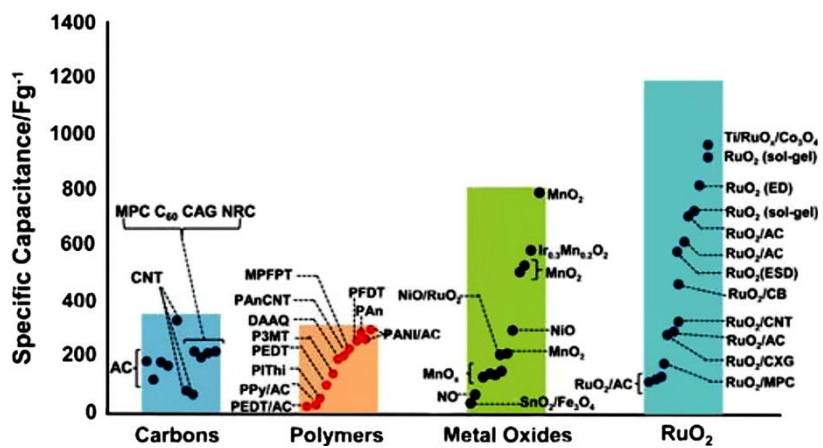


**Figure 3.** The capacitance performance for both carbon based EDLC electrodes and pseudocapacitor electrodes (including transition metal oxides and conducting polymers).<sup>31-32</sup> Copyright 2008, the electrochemical society.

### 1.1.2 Manganese oxide as active material of supercapacitors

$\text{MnO}_x$  has been studied as an active material for a long time because it is clearly noteworthy, displaying fine specific capacitance (200 – 600 F/g) and reversible charge–discharge feature with its natural abundance and low cost.<sup>10, 35-36, 43-44</sup>  $\text{MnO}_2$  with  $\gamma$ -phase has long been used as active cathode materials in  $\text{Zn}/\text{MnO}_2$  alkaline cells by Leclanche's group in the 1860s. After inventing the lithium ion batteries,  $\text{MnO}_2$  and spinel  $\text{Li}_{1-x}\text{MnO}_2$  received a lot of interest. In 1999, the use of  $\text{MnO}_2$  as electrochemical active materials for electrochemical energy storage continued to expand to electrochemical supercapacitors.<sup>45</sup> Lee and Goodenough initially reported that amorphous  $\text{MnO}_2$  electrode demonstrated electrochemical response in aqueous electrolyte and exhibited specific capacitance of around 200 F/g.<sup>46</sup> Afterward, interest in  $\text{MnO}_2$  as active materials of supercapacitors has been increasing consistently and  $\text{MnO}_2$  become one of the most attractive electrode materials.

There are many synthesis methods for  $\text{MnO}_2$  including sol-gel,<sup>47</sup> thermal oxidation,<sup>48</sup> and chemical coprecipitation<sup>49</sup>. Manganese oxides occur at least 30 different crystal structures (**Figure 4**).<sup>50</sup> As far as the chemical valence states of manganese oxide are concerned, it has different oxidation states (2+, 3+, 4+, and 6+). Generally, the phase change of manganese oxide appears at different temperatures ( $\text{MnO}_2$ ,  $\text{Mn}_2\text{O}_3$ ,  $\text{Mn}_3\text{O}_4$ , and  $\text{MnO}$ ). Moreover, electrochemical properties of  $\text{MnO}_x$  can be changed in accordance with various structures. Thus, electrochemical properties can be tuned by controlling the phase of  $\text{MnO}_x$ .



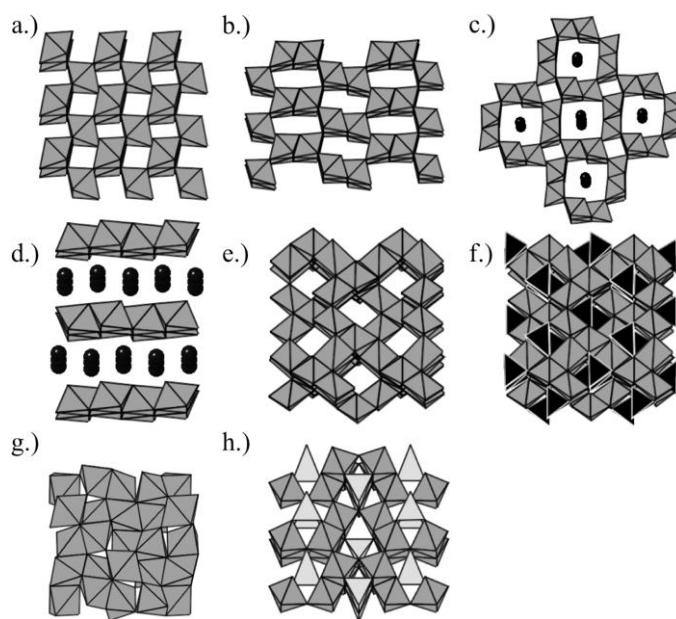


**Figure 4.** Polyhedral representation of the eight Mn oxides reported : (a)  $\beta$ -MnO<sub>2</sub>, (b) R-MnO<sub>2</sub>, (c)  $\alpha$ -MnO<sub>2</sub>, (d)  $\delta$ -MnO<sub>2</sub>, (e)  $\lambda$ -MnO<sub>2</sub>, (f) LiMn<sub>2</sub>O<sub>4</sub>, (g) Mn<sub>2</sub>O<sub>3</sub>, and (h) Mn<sub>3</sub>O<sub>4</sub>. The light, dark, and black polyhedral represent Mn<sup>2+</sup> tetrahedral, Mn<sup>3+</sup> and Mn<sup>4+</sup> octahedral, and Li<sup>1+</sup> tetrahedral, respectively. And black spheres represent K<sup>+</sup> ions.<sup>50</sup> Copyright 2011, Journal of the American Chemical Society.

### 1.1.3 Effect of electrode structure

Despite these favorable features of  $\text{MnO}_x$ , it has the poor electric conductivity ( $\sim 10^{-6}$  S/cm) and stability. These limitations cause the low capacitance value (typically in the range of 10-102 F/g) and unsatisfactory performance to fulfill the high-power performance requirements. Therefore, it is still a challenge to improve these limitations. In order to overcome these limitations, developments of the new materials are important. Moreover, efforts including creation of new electrode structure, generation of pore size distribution and deposition of electroactive metallic particles or conduction polymers are urgently needed. Furthermore, the redox reactions only occur on the surface of the active materials. Efforts have been made to produce the nanostructured pseudocapacitive materials in order to increase the active surface area and shorten the electron diffusion length.<sup>51-53</sup> Nanostructured materials have received considerable attention due to the remarkable electrical, mechanical, optical properties and high active surface area. Recent trends in supercapacitors involved the development of electrode with high surface area to enhance the performance of the capacitance and conductivity. Awareness has been focused on nanostructured materials including aerogels,<sup>54</sup> nanofibers, and nanotemplates<sup>52</sup>. Among a lot of nanostructures, 3D porous electrodes are known to exhibit a superior capacitance due to increased specific surface area and enhanced access of the electrolytes to the surface of porous electrode materials. Supercapacitors with 3D porous electrode were reported in recent years. 3D porous electrodes exhibited higher performance than that of normal electrodes. For example, Lang's group reported supercapacitor obtained by depositing  $\text{MnO}_2$  on the nanoporous gold substrate which improves fast ion diffusion and electron transport between the  $\text{MnO}_2$  and the electrolytes. This electrode demonstrated high specific capacitance of  $\sim 1145$  F/g for  $\text{MnO}_2$ .<sup>55</sup> And  $\text{MnO}_2$ -CNT-sponge supercapacitor reported by Alshareef et al. indicated that the specific capacitance of this composite was reached 1230 F/g.<sup>56</sup> In addition, the  $\text{MnO}_2$ -CNT-sponge supercapacitors showed only 4% loss after 10000 cycles at current density of 5 A/g. Thus 3D porous structure for supercapacitors can raise the electrochemical performance.

## 1.2 Electrospinning

Electrospinning can form electrode of the three-dimensional porous structure with one-dimensional nanofibers (NFs) and is known as inexpensive and efficient technique. Electrospinning technique first examined by Zeleny in 1914 and patented by Formhals in 1934, was initially exclusively applied to polymers.<sup>57</sup> Electrospinning has the advantages of simplicity, efficiency, low cost, high yield and high degree of reproducibility of the obtained materials. Furthermore, electrospinning technique can not only make the polymer, metal oxide NFs with various components, but also produce the NFs with unique structure such as hollow, core-shell, porous structure.<sup>58-60</sup> **Figure 5** illustrates a schematic picture of the electrospinning method. The electrospinning consists of three major components including the high voltage power supply, a needle, and the collector. The solution can be provided through the syringe pump at controllable rate. When applying a high voltage, the pendent polymer drop at the nozzle will become highly electrified and then the induced charges are evenly distributed over the surface of polymer drop. As a result, the drop will undergo two major electrostatic forces which are the electrostatic repulsion between the surface charges and the Coulombic force exerted by the external electric field. Under these electrostatic interactions, the polymer drop will be deformed into a conical shape generally known as the Taylor cone.<sup>61-64</sup> When the strength of electric field has exceeded a threshold value, the electrostatic force can overcome the surface tension of the polymer solution. Through process, the liquid jet can release from the nozzle and then this electrified jet experiences a stretching and whipping process. During process, liquid jet is continuously elongated and the solvent is evaporated. The diameter of fibers can be formed from hundreds of micrometers to tens of nanometers. The charged fiber is often deposited as a randomly arranged, non-woven mat on the grounded collector. Due to the relatively simple and easy process, more than 50 different types of organic polymers have already been reported as fibers with a wide range of diameters.<sup>61-63</sup> Though the setup for electrospinning method is very simple, the spinning mechanism is rather complicated. Before 1999, producing the ultrathin and uniform fibers by electrispinning process was often attributed to the splitting or splaying of the electrified jet as a result of repulsion between surface charges.<sup>61</sup> In recently researchers demonstrated that the thinning of a jet during electrospinning process is mainly caused by the bending instability related to the electrified liquid jet.<sup>65-67</sup> **Figure 6A** is the photograph of a spinning jet. This photograph shows that the jet was initially a straight line and then became unstable. It seems that the cone-shaped, instability region is composed of multiple jets. Nevertheless, as shown **Figure 6B**, the conical envelope consists of only single fiber rapidly bending or whipping.<sup>67</sup>

Based on experimental examination and electrohydrodynamic theories, mathematical models have been studied by several researchers to examine the electrospinning process. Reneker's group presented the charged liquid jet as a system of connected, viscoelastic dumbbells and reported a good

explanation about the formation of bending instability.<sup>64, 66</sup> They also calculated the trajectory of the liquid jet through a linear Maxwell equation and the computed results were in agreement with the experimental results. In addition, Rutledge and co-workers thought about the jet as a long, slender object and developed a different model to explain the electrospinning phenomenon.<sup>68-70</sup> Their experimental and theoretical studies clearly indicated that the spinning process only concerns with whipping of a liquid jet. The whipping instability primarily results from the electrostatic interactions between the external electric field and the surface charges on the jet. The formation of fibers is mainly achieved by the stretching and acceleration of the fluid filament in the instability region. Especially electrospun NFs can be tunable by controlling some parameters and new setups.

Due to diversity of electrospun NFs in terms of materials, structures, architectures and functionalities, the use of the electrospinning method has been increased for the production of NFs and fabrics and membranes elaborated from them. Electrospun NFs could be applied to the extensive applications such as biosensors, nanoelectronics, fuel cells, solar cells, membranes, and capacitors (**Figure 7**).<sup>71-74</sup> Moreover, in recent years researches for energy systems such as fuel cells, Li-ion batteries, and supercapacitors have significantly increased especially (**Figure 8**).<sup>75</sup>

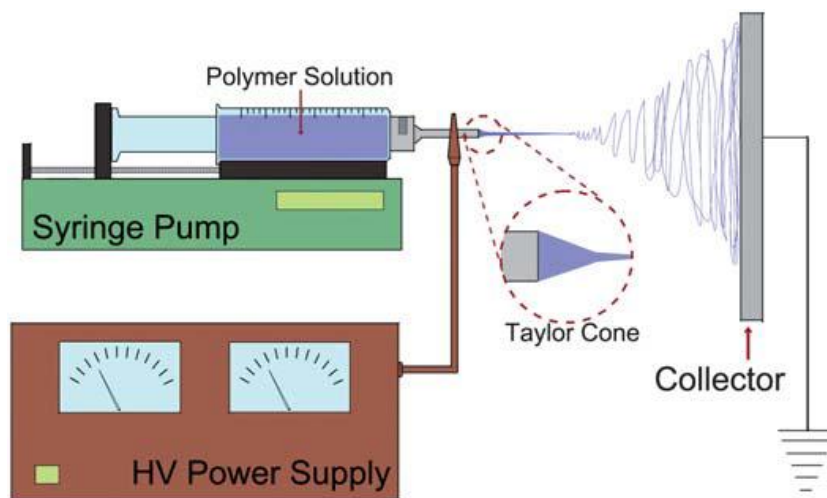


**Figure 5.** Schematic illustration of the electrospinning technique.<sup>75</sup>

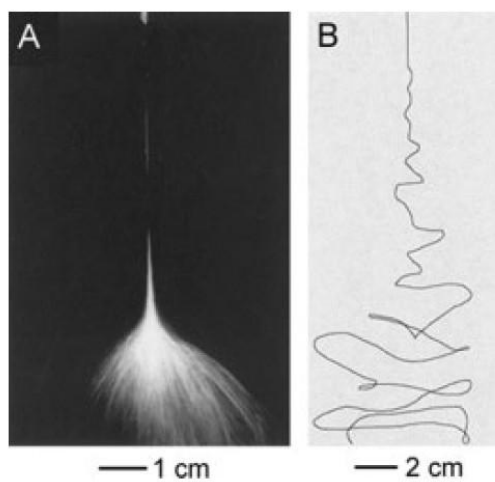


**Figure 6.** Photographs illustrating the instability region of a liquid jet electrospun from an aqueous solution of poly(ethylene oxide) (PEO). Note that the path of the jet shown in B has been traced to improve the visibility.<sup>67</sup> Copyright Elsevier Science, 2001.

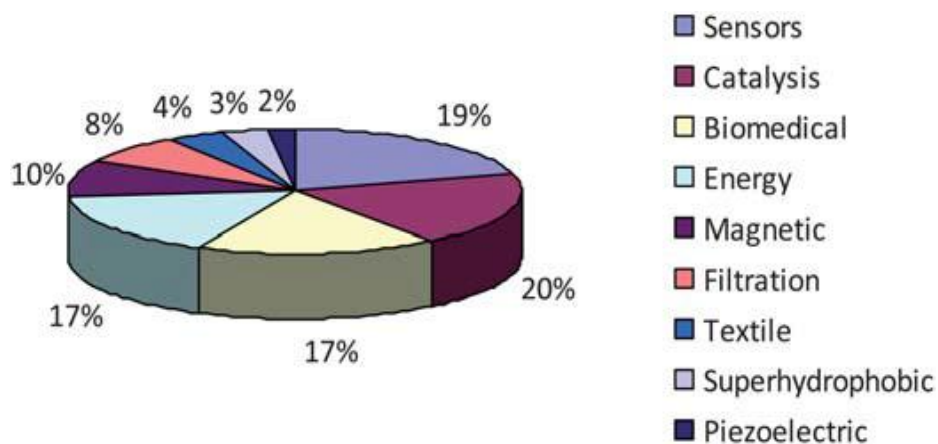


**Figure 7.** Relative proportion of publications in main areas of applications of electrospinning in the period of 2000–2010 (SciFinder data: keywords: electrospinning + type of application in the legend).<sup>75</sup>

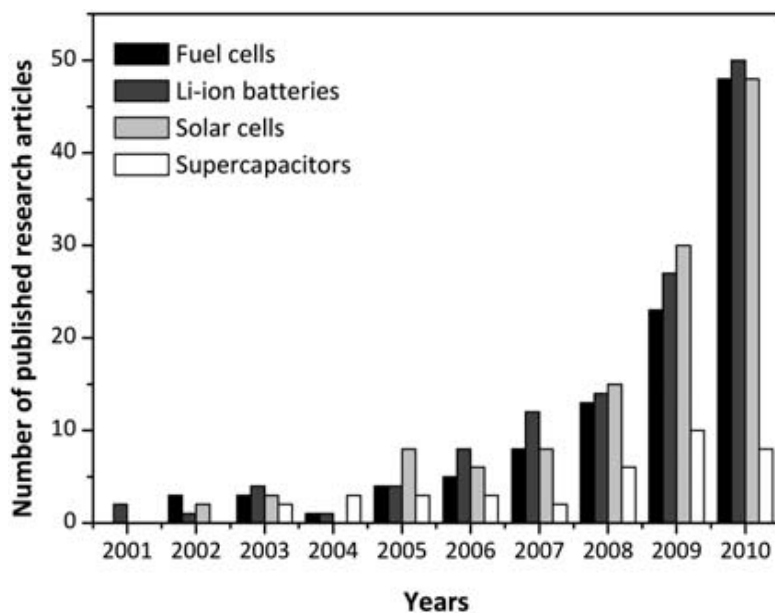


**Figure 8.** Number of research articles concerning electrospun nanofiber applications in energy devices published in the period of 2001–2010 (SciFinder data: keywords electrospinning + fuel cells, electrospinning + Li-ion batteries, electrospinning + solar cells, electrospinning + supercapacitors).<sup>75</sup>

### **1.2.1 Parameters of electrospinning**

The diameter and morphology of electrospun NFs are influenced by processing parameters such as the intrinsic properties of solution and the operational conditions. Firstly, the intrinsic properties of solution include the type of polymer, the conformation of polymer chain, viscosity (concentration), elasticity, electrical conductivity of polymer solution, the polarity, and surface tension of solvent. Secondly, the operational conditions are the applied voltage, the distance between nozzle and ground substrate, and the pumping rate of polymer solution. In addition, the environment conditions including the humidity and temperature of the surrounding have an effect on the morphology and diameter of electrospun NFs.<sup>61-63, 76</sup>

By controlling the various parameters, it is possible to obtain fibers having a morphology and diameter desired. The diameter of electrospun fibers can be adjusted by changing the parameters which there are the concentration of polymer, the electrical conductivity of solution, the applied voltage, and the pumping rate. In general, when increasing concentration of solution the electrospun fibers become thicker. Besides, thicker fibers can be obtained through fast pumping rate. While, if the conductivity of solution increased via adding salts, the diameter of fibers can be considerably decreased.<sup>76</sup> For example, Rutledge's group reported a model about the effect of various processing parameters. In this study, the diameter is considerably dependent on the interaction between surface tension and electrostatic repulsions.<sup>70</sup> The balance point might be concerned with feeding rate, the strength of electric field, and the surface tension of polymer solution. Through model in this paper, the expected diameters were corresponded with experimental results. Furthermore, change of the atmospheric composition and humidity can significantly influence diameters of fiber. Rangkupan and Reneker made thinner fibers of polypropylene (PP) under vacuum condition. The electrospun PP fibers obtained under vacuum are thinner than under normal pressure.<sup>77</sup>

### **1.2.2 Control of structure of electrospun NFs**

Fibers prepared by electrospinning generally exhibit round shape in cross section, solid interior, and smooth surface. In recent years, electrospun fibers with various structures were reported. For example, instead of usually round shape, electrospun fiber of ribbon-like structures with rectangular cross section was reported by Reneker's group.<sup>78-80</sup> In this paper, electrospun fibers with ribbon-like structure were obtained by the rapid evaporation of the solvent and then remaining solvent disappeared by diffusion through the skin. Thus, the shape of electrospun fiber could be changed by controlling the solvent of solution.

Electrospinning technique can produce fibers with specific structures such as hollow, porous, and core/shell. It is possible to make the core/shell NFs by using a polymer solution comprising two polymers which will phase separate. For instance, Yarin and co-workers have shown that electrospun

NFs with core/shell structure could be prepared by co-electrospinning of two different polymer solutions via two coaxial capillaries (**Figure 9**).<sup>81</sup> In order to fabrication of the continuous and uniform fibers with core/shell structure, it is important to two solutions should have immiscibility. But, it will be difficult to obtain core/shell fibers. More studies are still needed to achieve the control of desired structure.

As well as electrospun fibers with core/shell structure, electrospun fibers with porous structure have also been many reported. How to make fibers with porous structure, there are two slightly different approaches. One of two approaches was based on the selective elimination of a component from fibers prepared of a blend material or composite. Another involved the use of phase separation of different polymers during electrospinning process. Wendorff's group reported the structural change of fibers consisting of PVP and PLA through selective removal (**Figure 10**).<sup>82</sup> This study demonstrated that when there existed equal amounts of the two polymers into solution, the fibers became highly porous structure. And when increasing ratio of one polymer in solution, fibers formed more compact structure. Thus, by changing the ratio of polymers, porosity of fibers can be controlled. It is possible to adjust the pore size and density of electrospun fibers by changing the processing parameters.



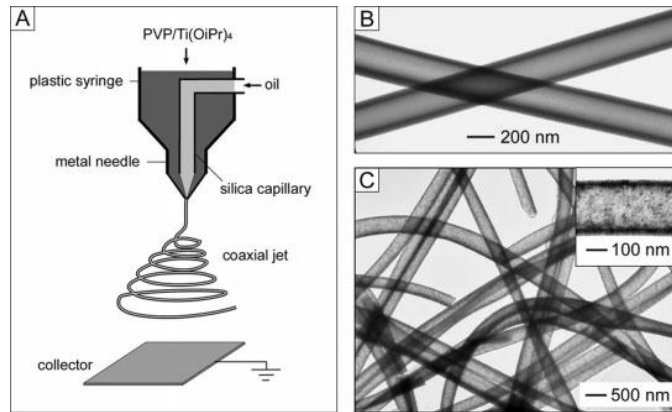


**Figure 9.** (A) Schematic illustration of the setup used to prepare the hollow NFs by electrospinning. It concerns the use of a spinneret composed of two coaxial capillaries, through which mineral oil and an ethanol solution including titanium tetraisopropoxide and PVP were concurrently ejected to form a compound jet. (B) TEM image of the as-spun hollow NFs whose walls were made of a composite of amorphous TiO<sub>2</sub> and PVP. (C) TEM image of anatase hollow NFs that were obtained by annealing the composite nanotube at 500 °C in air.<sup>81</sup> Copyright American Chemical Society, 2004.

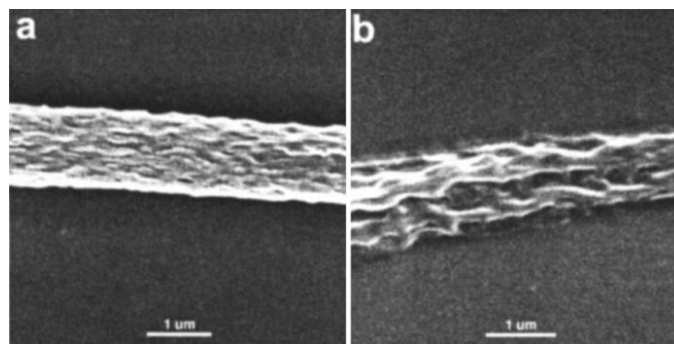


**Figure 10.** SEM micrographs of PVP/PLA 1:1 fibers : (a) residual PLLA fiber after selective removal of PVP, (b) residual PDLA fiber after selective removal of PVP.<sup>82</sup> Copyright Polymer Engineering and science

### 1.2.3 Preparation of electrospun inorganic NFs

Electrospinning has been primarily used to fabrication of organic polymer NFs since electrospinning solution should have viscoelastic behavior. The many groups informed that composite or inorganic NFs could be fabricated by using sol-gel precursor solution. Subsequently, electrospinning technique has been presenting in an effective way to form composite and inorganic NFs. Particularly, inorganic nanofibers can be simply prepared by electrospinning technique which use inorganic/polymer solution obtained by mixed. Inorganic/polymer solution is very important to form inorganic fibers. Diameter of electrospun inorganic fibers was usually several hundred nanometers and it is possible to reduce the diameter of fibers by adjusting parameters of electrospinning process. Polymer/inorganic fibers prepared by electrospinning could become ceramic fibers by removing the polymer through calcination of polymer/inorganic fibers in air. This process has been successfully extended to form many other ceramic fibers such as  $\text{SiO}_2$ ,  $\text{SnO}_2$ ,  $\text{NiFe}_2\text{O}_4$  and  $\text{LiCoO}_2$ . Moreover, PVP, poly(vinyl alcohol) (PVA), poly(vinyl acetate) (PVAc), and poly(ethylene oxide) (PEO) have usually been used as the polymer matrixes to host inorganic precursors.<sup>83-86</sup> As a result, inorganic NFs such as  $\text{Al}_2\text{O}_3$ ,  $\text{CuO}$ ,  $\text{NiO}$ ,  $\text{ZnO}$ , and  $\text{MgTiO}_3$  could have been generated as 3D structure. As shown these studies, electrospinning technique may provide an effective way to prepare inorganic NFs. Furthermore, electrospun inorganic NFs can be used for various applications, for instance, as active units in sensing, as membranes of separation, as supports for catalysis, and as electrode active materials of energy conversion and storage systems.

### 1.2.4 Electrospun fibers for supercapacitors

Electrospinning has been reported as effective method to fabricate electrode and separator materials with highly porous and nanofibrous structure for supercapacitors. Recently, many researchers have informed that electrospun carbon NF mat could be used as electrode for supercapacitors instead of normal carbon electrode. There are many precursors to prepare carbon NF mat. Among them, PAN is the most used as precursors.<sup>87-89</sup> Carbon NF mat obtained by electrospinning and calcination have high porosity and surface area. It can improve the specific capacitance at high current density due to the faster transport of ions.<sup>90</sup> Moreover, to enhance the capacitance of carbon electrode, some studies reported the composite consisted of electrospun carbon mat and other components such as silver,<sup>91</sup> nickel,<sup>92</sup> or CNTs<sup>93</sup>. This composite exhibits improved capacitance due to increasing the conductivity of material. In addition, fiber mat of transition metal oxides such as  $\text{RuO}_2$ ,  $\text{MnO}_x$ , and  $\text{NiO}$  can be prepared by electrospinning technique as well as carbon NF mat. For instance, capacitor based on  $\text{RuO}_2$  electrodeposited onto electrospun  $\text{TiO}_2$  nanorods demonstrated a high rate capability.<sup>94</sup> In another case, capacitor was fabricated by depositing a thin  $\text{RuO}_2$  layer onto the crystalline  $\text{RuO}_2$  nanofibrous mat. This electrode showed a high specific capacitance and high rate capability.<sup>95</sup>

Through the reported studies, electrodes with highly porous and conductive electrospun mat for supercapacitors have demonstrated high specific capacitance and rate capability. These results were attributed to the unique porous structure and the reduced interfacial resistance of between the electrode material and the electrolyte. The porous structure provides high surface area and high porosity leading an efficient permeability of the electrolyte and a good surface activity. In addition, it offers a facile ion pathway and the latter a fast electron pathway.

## II. EXPERIMENTS

### 2.1 Preparation of electrospun MnO<sub>x</sub> NFs

**Figure 11** illustrates the procedure to produce the electrospun MnO<sub>x</sub> NF in this paper. Poly(N-vinyl pyrrolidone) (PVP) solution was prepared by dissolving PVP powder ( $M_w$  1,300,000 g/mol) in deionized water (20 wt%). Then, Mn(OAc)<sub>2</sub>/PVP solution was prepared by dissolving manganese acetate (20 wt%) in PVP solution. This solution was stirred for at least one day in order to obtain homogeneously distributed solutions. The solution obtained was injected from a syringe and syringe was fixed in syringe pump. The size of the needle in the electrospinning was 25 G, and the needle was connected to high-voltage power supply. The feeding rate of solution was fixed at 10  $\mu$ l/min, and the distance between the needle and collector was 10 cm and the applied voltage was 25 kV. The electrospun Mn(OAc)<sub>2</sub>/PVP NFs were annealed at different temperatures (400, 500, 600 and 700 °C) to remove the polymer matrix and result in the MnO<sub>x</sub> NFs.

### 2.2 Electrochemical measurement

Electrochemical performance of the electrospun MnO<sub>x</sub> NFs were carried out with a standard three-electrode test cell with 0.5 M Na<sub>2</sub>SO<sub>4</sub> aqueous solution as electrolyte. Platinum (Pt) wire and Ag/AgCl were used as a counter and reference electrode, respectively. The characterization of the electrochemical performance for the obtained MnO<sub>x</sub> electrode was investigated through a VMP3 electrochemical potentiostat (BioLogic Inc.). Cyclic voltammograms (CVs) and the galvanostatic charge-discharge test were carried out with a potential window from -0.2 to 0.8 V versus Ag/AgCl in 0.50 M Na<sub>2</sub>SO<sub>4</sub> electrolyte with scan rates from 5 to 200 mV/s and a current density of 1 A/g. In order to internal resistance of MnO<sub>x</sub> electrode, measurement of electrochemical impedance spectroscopy (EIS) was measured in frequency range of 100 kHz-100 mHz.

### 2.3 Characterizations

The morphology and diameter of the prepared MnO<sub>x</sub> NFs were examined using a field emission scanning electron microscopy (FESEM, FEI, Nanonova 230) and transmission electron microscopy (TEM, JEOL JEM-2100 accelerating voltage of 200 kV, Gatan CCD camera). X-ray diffraction (XRD) measurement was employed by a high-power X-ray diffractometer (Rigaku Co., D/MAZX 2500V/PC) from 10° to 80°.

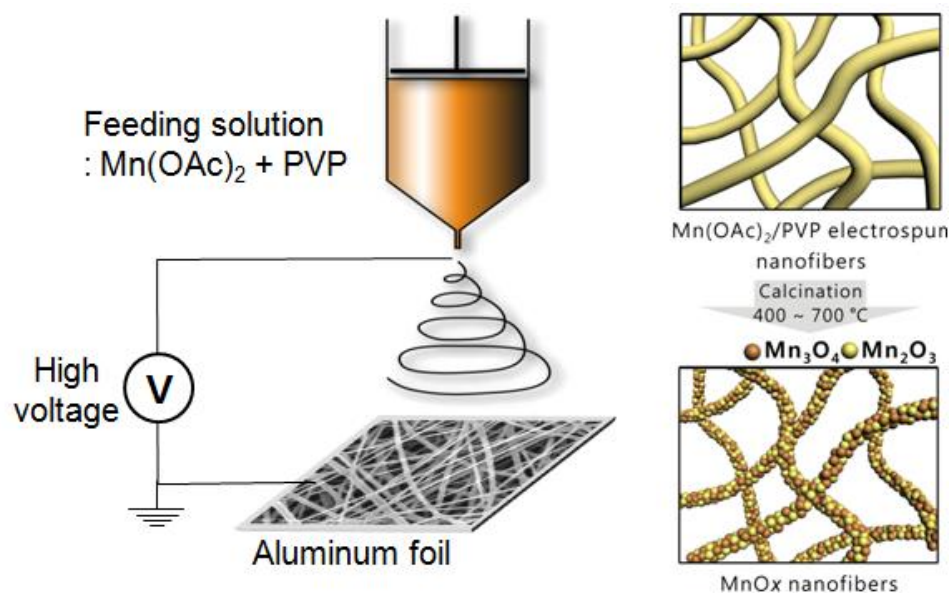


**Figure 11.** Schematic illustration for the fabrication of the electrospun NFs and subsequent calcination process for hybrid MnO<sub>x</sub> NF supercapacitors.

### III. RESULTS AND DISCUSSION

#### 3.1 Characterization of Electrospun MnO<sub>x</sub> NFs

Initially, Mn(OAc)<sub>2</sub>/PVP NFs were successfully fabricated by electrospinning using the procedures outlined in the experimental section. **Figure. 12** shows the SEM images and diameter distribution of the as-spun Mn(OAc)<sub>2</sub>/PVP NFs and the MnO<sub>x</sub> NFs formed after calcination at different temperatures from 400 to 700 °C. As shown in Fig. 1a, as-spun Mn(OAc)<sub>2</sub>/PVP NFs were randomly oriented in a continuous, 3D, porous internal structure. The range of NF diameters in the sample was relatively narrow, and no beads were formed. The degradation of the PVP in as-spun fibers upon calcination is clearly indicated in the thermogravimetric analysis (TGA) (**Figure 13**). The polymeric component (PVP) was completely degraded at ~400 °C in air. The initial drastic decrease of the diameter of NFs occurred at calcination around 400 °C due to the removal of PVP and organic component in Mn(OAc)<sub>2</sub>, which comprise ca. 90 wt% of the as-spun fibers. Accordingly, the as-spun Mn(OAc)<sub>2</sub>/PVP NFs were calcined above 400 °C in air. After calcination at different temperatures, the 3D porous structure was retained without significant structural deformation. However, the diameter of MnO<sub>x</sub> NFs decreased after calcination owing to the removal of the PVP matrix and the crystallization of MnO<sub>x</sub>; for example, the average diameter of as-spun fiber decreased from 135 ± 18 nm to 72.3 ± 14.3 nm (400 °C), 64.2 ± 12.6 nm (500 °C), 52.7 ± 8.9 nm (600 °C) and 54.5 ± 6.9 nm (700 °C), respectively.

Various forms of manganese oxide such as α-MnO<sub>2</sub>, δ-MnO<sub>2</sub>, λ-MnO<sub>2</sub>, Mn<sub>2</sub>O<sub>3</sub>, and Mn<sub>3</sub>O<sub>4</sub> are known to exist depending on the conditions of annealing.<sup>50</sup> We further characterized the phase composition of MnO<sub>x</sub> NFs after calcination by XRD (**Figure. 14**). The XRD patterns of MnO<sub>x</sub> fibers calcined at different temperatures corresponded to either Mn<sub>3</sub>O<sub>4</sub> (JCPDS 024-0734) or Mn<sub>2</sub>O<sub>3</sub> (JCPDS 073-1826), or a combination of both. The NFs calcined at 400 °C adopted the tetragonal Mn<sub>3</sub>O<sub>4</sub> phase exclusively (**Figure. 14a**). Above 400 °C, Mn<sub>3</sub>O<sub>4</sub> transformed into the more oxidized Mn<sub>2</sub>O<sub>3</sub> as the calcination temperature increased, giving mixed-phase nanofibers (MnO<sub>x</sub> NFs) (**Figure. 14b and 14c**). We correlated the compositional ratio between Mn<sub>3</sub>O<sub>4</sub> to Mn<sub>2</sub>O<sub>3</sub> on the basis of the main XRD peak intensity ratio, assuming there is no other crystalline phases of MnO<sub>x</sub> NFs. Specifically, the ratio of Mn<sub>3</sub>O<sub>4</sub> to Mn<sub>2</sub>O<sub>3</sub> decreased from 100:0 (400 °C) to 68:32 and 18:82 at 500 and 600 °C, respectively, and at 700 °C, the initial Mn<sub>3</sub>O<sub>4</sub> phase transformed into Mn<sub>2</sub>O<sub>3</sub> completely.

We further investigated the internal structure of the sample annealed at 500 °C by TEM and electron mapping by energy-dispersive spectroscopy (EDS) to confirm the existence of both Mn<sub>3</sub>O<sub>4</sub> and Mn<sub>2</sub>O<sub>3</sub> phases (**Figure. 15**). The hybrid MnO<sub>x</sub> NFs were composed of granular nanoparticles with diameters of 61 ± 12 nm that were connected along the framework of the NFs. In addition, the high-resolution TEM (HRTEM) image revealed that MnO<sub>x</sub> NFs were crystalline. The crystalline lattice fringes of 0.24 and 0.49 nm corresponded to the primary reflection of the (211) and (101) peak of

Mn<sub>3</sub>O<sub>4</sub>, respectively. Furthermore, the electron diffraction pattern of a selected area of MnO<sub>x</sub> also exhibited a lattice fringe of 0.384 nm, which is associated with the (121) peak of Mn<sub>2</sub>O<sub>3</sub> (**Figure. 15b**). We also confirmed that Mn and O were distributed homogeneously within the electrospun MnO<sub>x</sub> NFs by EDS (**Figure. 15c**). Overall, HRTEM image and the electron diffraction pattern confirmed the presence of mixed phase of Mn<sub>3</sub>O<sub>4</sub> and Mn<sub>2</sub>O<sub>3</sub> in the MnO<sub>x</sub> NFs calcined at 500 °C, in good agreement with the result of XRD.

### 3.2 Electrochemical performance of electrospun MnO<sub>x</sub> NFs

We investigated the electrochemical properties of hybrid MnO<sub>x</sub> NFs annealed at different temperatures by cyclic voltammetry (CV) measurements. All CV data were measured in 0.5 M Na<sub>2</sub>SO<sub>4</sub> electrolytes at potential intervals from -0.2 to 0.8 V with platinum wire and Ag/AgCl as a counter and reference electrode, respectively (**Figure. 16**). All MnO<sub>x</sub> NF electrodes displayed the typical broad redox peaks in the potential range investigated. In particular, the CV curves of MnO<sub>x</sub> annealed at 400 and 500 °C clearly showed the redox transitions of MnO<sub>x</sub> characteristic pseudocapacitive behavior. The specific capacitance values obtained from CV ( $C_{sp,CV}$ ) were determined to be 140.1, 214.7, 69.0, and 46.3 F/g for electrodes prepared from MnO<sub>x</sub> NF calcined at 400, 500, 600, and 700 °C, respectively, at a scan rate of 10 mV/s. Interestingly, among all electrodes prepared from MnO<sub>x</sub> NFs, the one annealed at 500 °C exhibited the highest  $C_{sp,CV}$  value. In addition, the linear response of the capacitive current to changes in the potential scan rate revealed that the redox behavior of the system was highly reversible (inset in **Figure. 16b**). Therefore, the capacitance of each electrode strongly depended on the compositional ratio of Mn<sub>2</sub>O<sub>3</sub> and Mn<sub>3</sub>O<sub>4</sub>; for example, Mn<sub>3</sub>O<sub>4</sub>-rich phases (NFs calcined at 400 and 500 °C) exhibited higher  $C_{sp,CV}$  and  $C_{sp,G}$  than Mn<sub>2</sub>O<sub>3</sub>-rich phases (NFs calcined at 600 and 700 °C). Also, the sample annealed at 500 °C with a mixed phase of Mn<sub>2</sub>O<sub>3</sub> and Mn<sub>3</sub>O<sub>4</sub> showed a higher  $C_{sp,CV}$  and  $C_{sp,G}$  than that of pure Mn<sub>3</sub>O<sub>4</sub> sample annealed at 400 °C.

We further evaluated the supercapacitor performance of all MnO<sub>x</sub> electrodes by the galvanostatic charge–discharge test under an identical three-electrode system. The non-linear charge–discharge curves are characteristic for the pseudocapacitive behavior (**Figure. 16d**). The specific capacitance based on the galvanostatic ( $C_{sp,G}$ ) is calculated by the following equation:

$$C_{sp,G} \text{ (F/g)} = (i \times \Delta t) / (\Delta E \times m)$$

where  $i$  is the discharge current (A),  $\Delta t$  is discharge time (s),  $\Delta E$  is the voltage difference (V), and  $m$  is the active mass of electrode (g). The galvanostatic test-based specific capacitance ( $C_{sp,G}$ ) of the MnO<sub>x</sub> electrodes annealed at 500 °C was calculated to be 367 F/g at a current density of 1 A/g, the highest

among all samples. The trends of the galvanostatic and CV measurements agree well with each other, even though the values for the latter are higher.

The value obtained from galvanostatic measurements is comparable to the value (highest capacitance of 230.5 F/g at a scan rate of 25 mV/s at calcination temperature of 300 °C) published in a recent study by Lin et al., in which the supercapacitor properties of different phases of MnO<sub>x</sub> film coated by a sol-gel process and annealed at 250 – 400 °C were evaluated.<sup>96</sup> In contrast, the MnO<sub>x</sub> NFs prepared in this study exhibited considerably higher capacitance than the MnO<sub>x</sub> film prepared by a sol-gel process owing to their unique 3D internal structures.

Our study also suggested that electrospinning permits the creation of 3D electrodes that are characterized by both increased surface area and efficient and fast ion transport between the electrode and electrolyte, thus enhancing the electrochemical properties of the supercapacitor.

The kinetics and interfacial resistance that are critical in the evaluation of the electrochemical reactions can be studied by electrochemical impedance spectroscopy (EIS). The EIS data can be fitted by an equivalent circuit consisting of a solution resistance ( $R_s$ ), a charge transfer resistance ( $R_{CT}$ ), a capacitance ( $C$ ), and Warburg impedance ( $Z_w$ ) (**Figure 17**). We thus investigated the charge transfer resistance ( $R_{CT}$ ) of all four MnO<sub>x</sub> NF electrodes in order to elucidate whether capacity was significantly dependent on the phase changes in MnO<sub>x</sub>.  $R_s$  and  $R_{CT}$  values obtained by fitting the data are present in **Table 2**. We determined that the  $R_{CT}$  value of MnO<sub>x</sub> electrode annealed at 500 °C (6 Ω) was far lower than those of the other three samples (118 Ω, 125 Ω, and 268 Ω at 400 °C, 600 °C, and 700 °C, respectively). This result indicates that the mixed phase of Mn<sub>3</sub>O<sub>4</sub> and Mn<sub>2</sub>O<sub>3</sub> exhibits a lower charge-transfer resistance, which accounts for the improved electrochemical performance of the supercapacitors. In addition to the above observation, we argue that the enhanced supercapacitive performance stems from the balance between the conductivity and capacitance of two different phases of MnO<sub>x</sub> NFs, such as Mn<sub>3</sub>O<sub>4</sub> and Mn<sub>2</sub>O<sub>3</sub>. It is known that the conductivity of the Mn<sub>2</sub>O<sub>3</sub> is relatively lower than that of Mn<sub>3</sub>O<sub>4</sub>, while the capacitance of the former is comparatively higher than that of latter.<sup>24, 35, 97-99</sup> Thus, the fine balance between the conductivity and capacitance of two different phases of MnO<sub>x</sub> NFs may result in the enhanced capacitance of the mixed phase MnO<sub>x</sub> NFs.<sup>100</sup> Although further in-depth analyses of the role of different phases within the electrospun fiber matrix of MnO<sub>x</sub> electrode are still required, the results presented here highlight the potential of electrospinning for producing electroactive 3D electrodes.



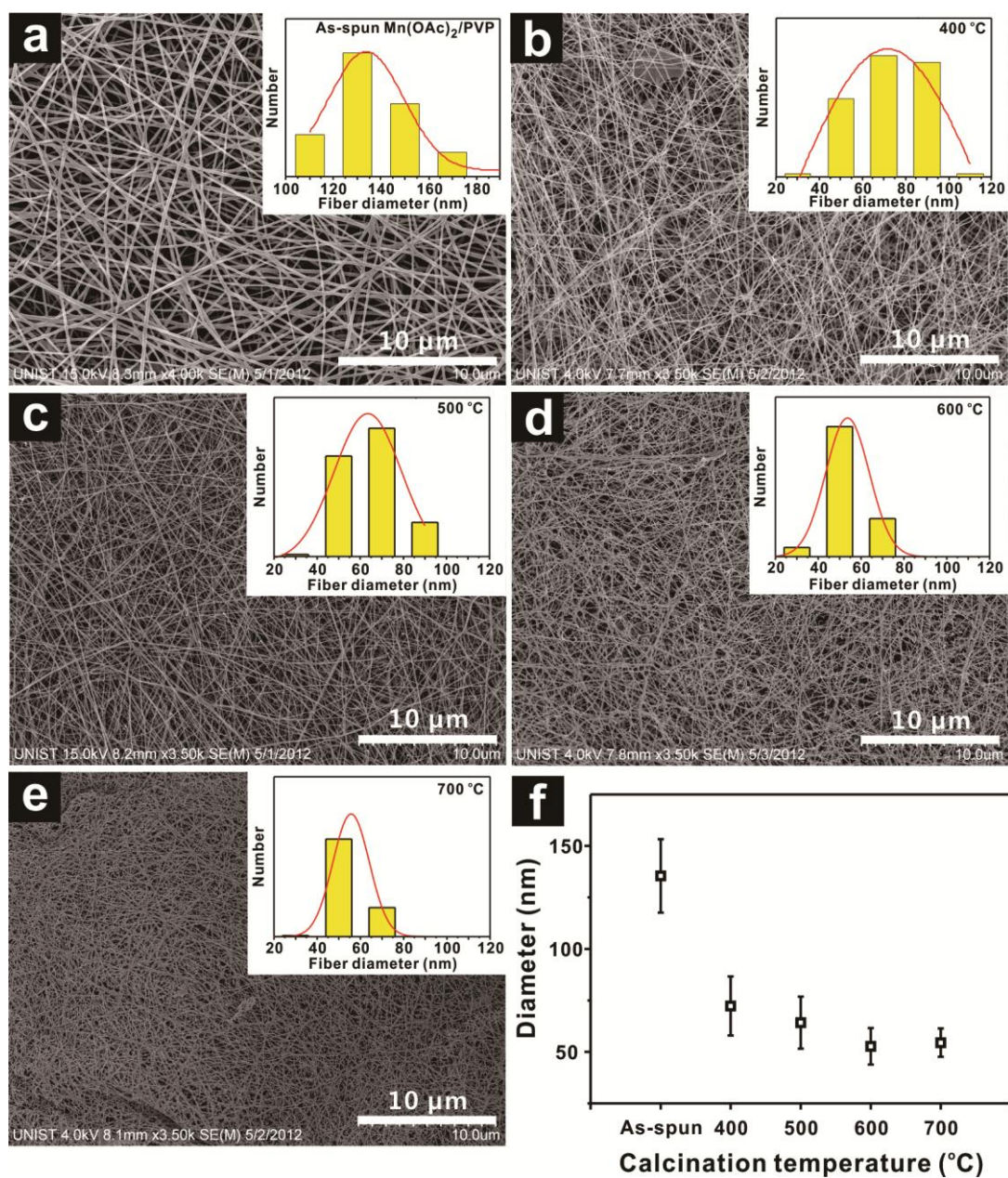


**Figure 12.** (a) SEM images of as-spun Mn(OAc)<sub>2</sub>/PVP NFs. (b-e) SEM images of MnO<sub>x</sub> NFs produced from the Mn(OAc)<sub>2</sub>/PVP NFs by calcining at (b) 400, (c) 500, (d) 600, and (e) 700 °C for 2 h in air. The inset graphs show the diameter distribution of each NF. (f) Plot of average diameter obtained from more than 50 individual SEM images as a function of the calcination temperature. The standard deviations are given as error bar.

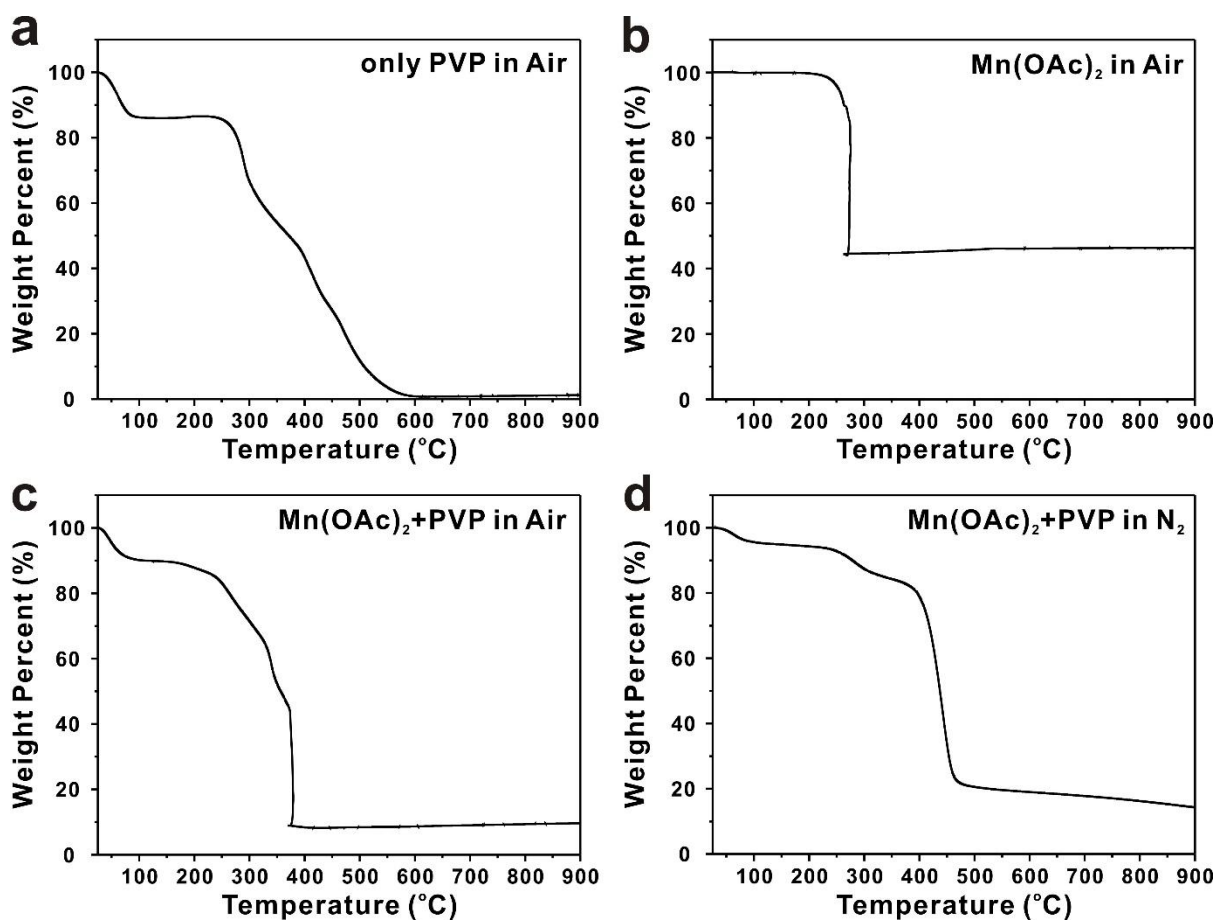


**Figure 13.** TGA curves of (a) pure electrospun PVP NFs prepared with PVP powder ( $M_w$  1,300,000 g/mol) in deionized water (20 wt%), (b)  $Mn(OAc)_2$  powder and (c, d) electrospun  $Mn(OAc)_2$ /PVP NFs which were made by dissolving a manganese acetate (20 wt%) in PVP solution (20 wt%). TGA plots were measured in (a - c) air and (d)  $N_2$  atmosphere at a heating rate of 5 °C/min.

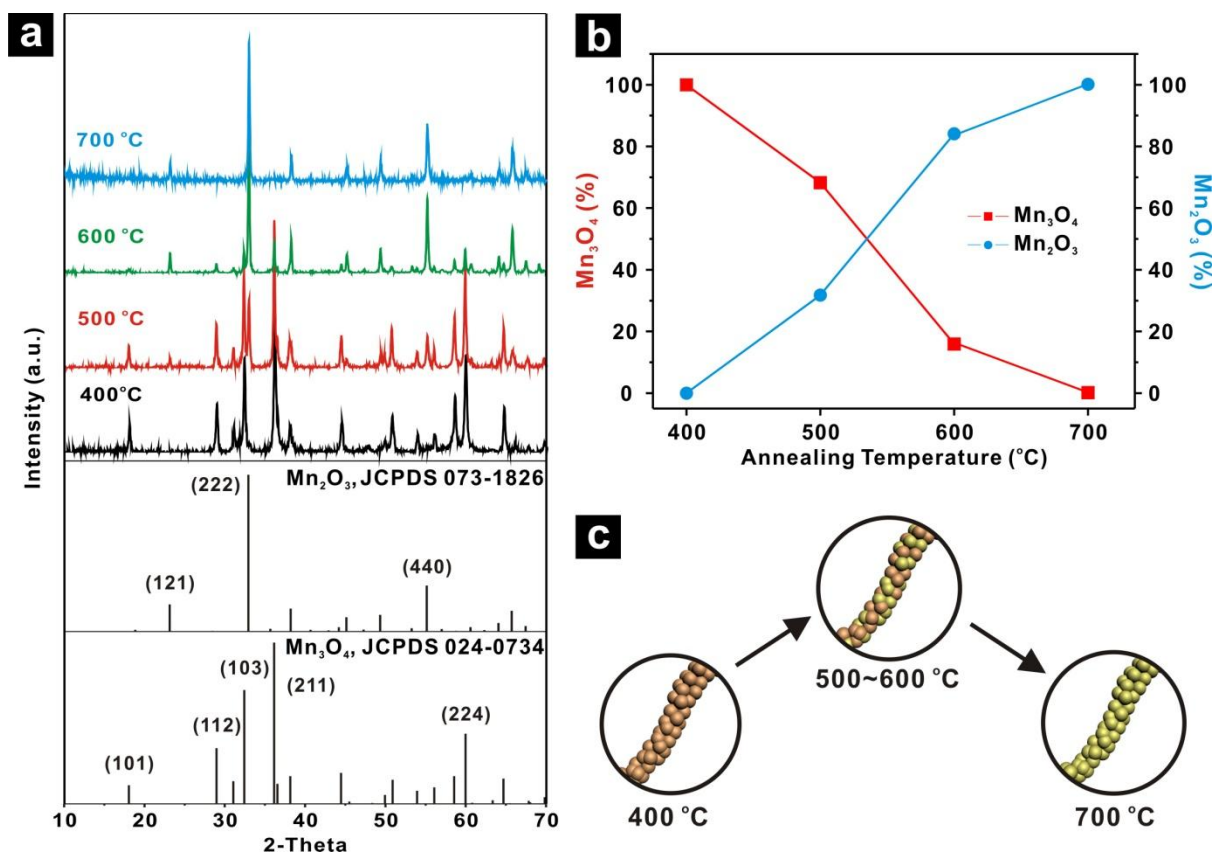


**Figure 14.** (a) XRD patterns of the MnO<sub>x</sub> NFs after calcining at 400-700 °C compared to the patterns of neat Mn<sub>3</sub>O<sub>4</sub> and Mn<sub>2</sub>O<sub>3</sub>. (b) Plot of relative phase compositions of MnO<sub>x</sub> NFs as a function of the calcination temperature. (c) Schematic representation of the phase changes of MnO<sub>x</sub> NFs as a function of the temperature.

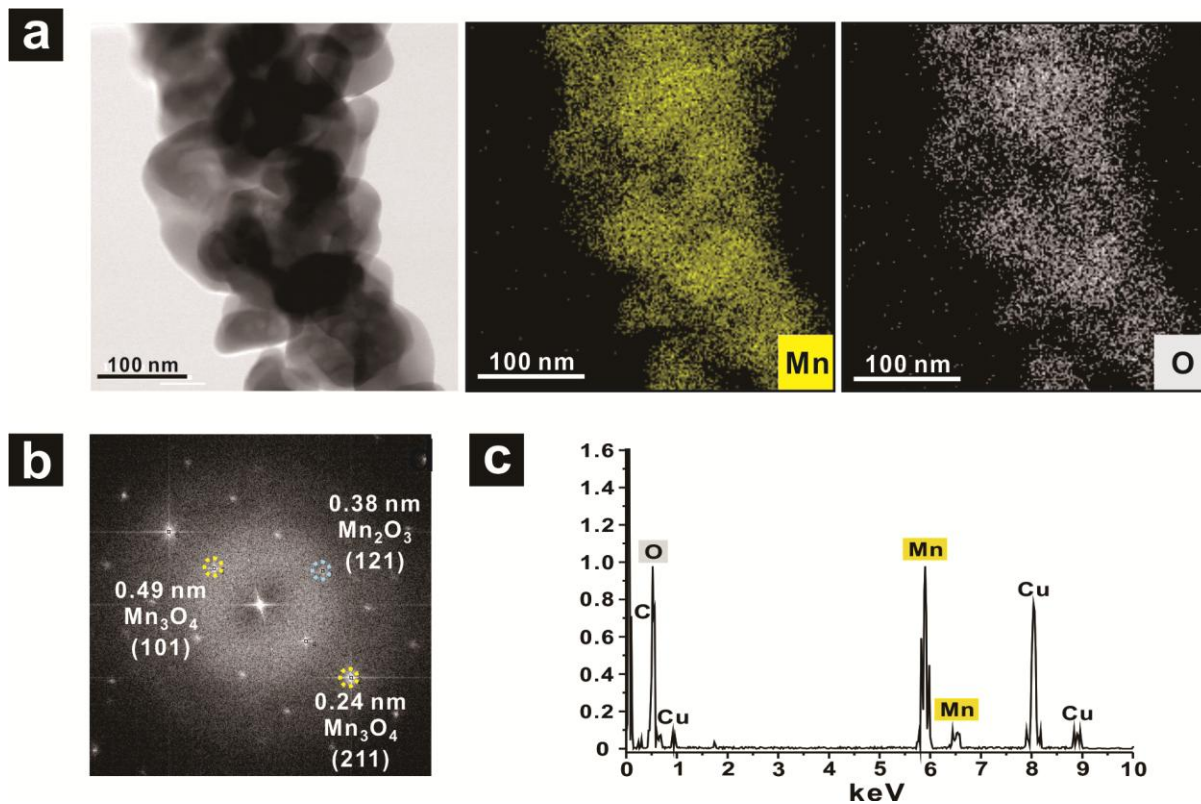


**Figure 15.** (a) TEM image, and (b) electron diffraction pattern of MnO<sub>x</sub> NFs calcined at 500 °C, (c) EDS mapping of Mn and O in MnO<sub>x</sub> NF calcined at 500 °C.

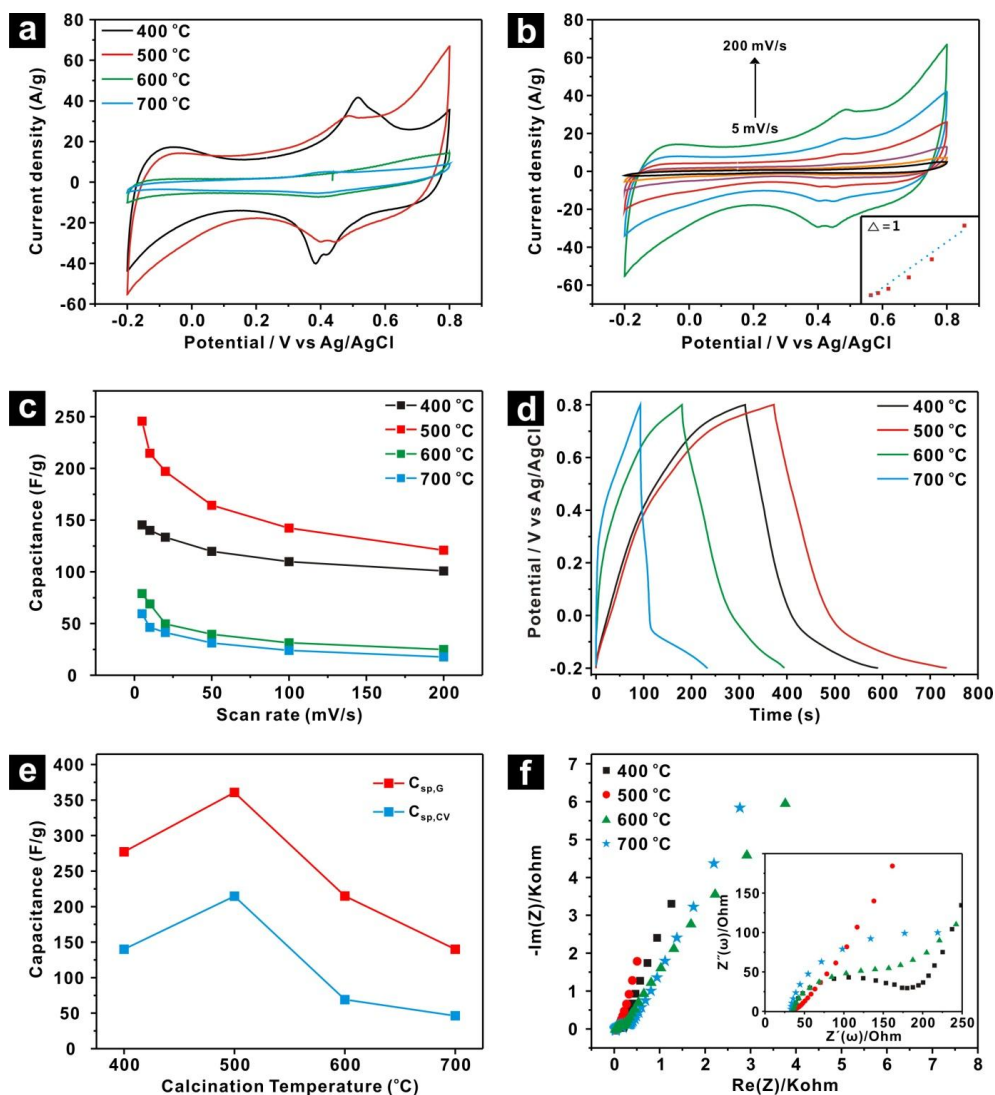


**Figure 16.** (a) Cyclic voltammety (CV) curves at a scan rate of 200 mV/s of all MnO<sub>x</sub> NFs calcined at the specified temperatures. (b) A plot of the current densities of the MnO<sub>x</sub> NFs clacined at 500 °C at scan rates from 5 to 200 mV/s. (c) Dependence of the capacitance on the calcination temperature. (d) Galvano charge-discharge curves of MnO<sub>x</sub> NFs calcined at the specified temperatures at a current density of 1 A/g. (e)  $C_{sp,CV}$  and  $C_{sp,G}$  of electrodes prepared from MnO<sub>x</sub> as a function of the calcination temperature. (f) Nyquist plots of the electrochemical impedance spectroscopy (EIS) for the electrospun MnO<sub>x</sub> electrodes as a function of the calcination temperature.

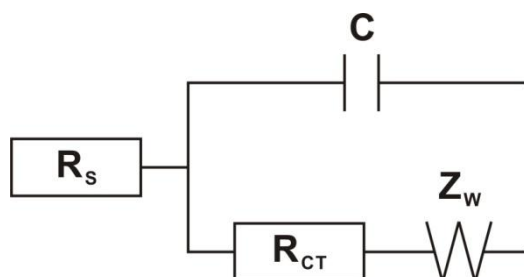


**Figure 17.** The equivalent circuit from the electrochemical impedance spectroscopy (EIS) analysis.

Calcination temperature ( $^{\circ}\text{C}$ )	$R_s$ ( $\Omega$ )	$R_{CT}$ ( $\Omega$ )
400	35.8	118
500	33.98	6
600	36.2	125
700	32.7	268

**Table 2.** EIS data of  $\text{MnO}_x$  NFs prepared at different calcination temperatures.

#### IV. Conclusion

We prepared the electrospun fibers of polyvinylpyrrolidone (PVP)/manganese acetate ( $\text{Mn}(\text{OAc})_2$ ) composite by using sol-gel processing and electrospinning technique. The as-produced inorganic nanofibers were annealed at different temperatures (400 to 700 °C) to remove the polymer matrix and result in the  $\text{MnO}_x$  nanofibers of varying composition of  $\text{Mn}_2\text{O}_3$  and  $\text{Mn}_3\text{O}_4$ . XRD measurements suggested that as-prepared  $\text{MnO}_x$  nanofiber changed from  $\text{Mn}_3\text{O}_4$  to  $\text{Mn}_2\text{O}_3$ , when the annealing temperature increased from 400 to 700 °C. We found that the capacitance of  $\text{MnO}_x$  nanofibers annealed at 500 °C is the highest (360.72 F/g at 1 A/g) among all samples with contained a mixed phase of  $\text{Mn}_2\text{O}_3$  and  $\text{Mn}_3\text{O}_4$ . Further electrochemical study will elucidate the potential of electrospun nanofibers of  $\text{MnO}_x$  for a promising supercapacitor application.

## References

1. Arumuganathar, S.; Irvine, S.; McEwan, J. R.; Jayasinghe, S. N., A novel direct aerodynamically assisted threading methodology for generating biologically viable microthreads encapsulating living primary cells. *J. Appl. Polym. Sci.* **2008**, 107, 1215-1225.
2. D'Amato, G., Environmental urban factors (air pollution and allergens) and the rising trends in allergic respiratory diseases. *Allergy* **2002**, 57, 30-33.
3. Veleirinho, B.; Rei, M. F.; Lopes-da-Silva, J. A., Solvent and concentration effects on the properties of electrospun poly(ethylene terephthalate) nanofiber mats. *J. Polym. Sci. Part B-Polym. Phys.* **2008**, 46, 460-471.
4. Whittingham, M. S., Lithium batteries and cathode materials. *Chem Rev* **2004**, 104, 4271-4301.
5. Arico, A. S.; Bruce, P.; Scrosati, B.; Tarascon, J. M.; Van Schalkwijk, W., Nanostructured materials for advanced energy conversion and storage devices. *Nat. Mater.* **2005**, 4, 366-377.
6. Conway, B. E., TRANSITION FROM SUPERCAPACITOR TO BATTERY BEHAVIOR IN ELECTROCHEMICAL ENERGY-STORAGE. *J. Electrochem. Soc.* **1991**, 138, 1539-1548.
7. Dunn, B.; Kamath, H.; Tarascon, J. M., Electrical Energy Storage for the Grid: A Battery of Choices. *Science* **2011**, 334, 928-935.
8. Simon, P.; Gogotsi, Y., Materials for electrochemical capacitors. *Nat. Mater.* **2008**, 7, 845-854.
9. Liu, R.; Duay, J.; Lee, S. B., Heterogeneous nanostructured electrode materials for electrochemical energy storage. *Chem. Commun.* **2011**, 47, 1384-1404.
10. Lee, J. W.; Hall, A. S.; Kim, J. D.; Mallouk, T. E., A Facile and Template-Free Hydrothermal Synthesis of Mn<sub>3</sub>O<sub>4</sub> Nanorods on Graphene Sheets for Supercapacitor Electrodes with Long Cycle Stability. *Chem. Mater.* **2012**, 24, 1158-1164.
11. Kotz, R.; Carlen, M., Principles and applications of electrochemical capacitors. *Electrochim. Acta* **2000**, 45, 2483-2498.
12. Zhang, L. L.; Zhao, X. S., Carbon-based materials as supercapacitor electrodes. *Chem. Soc. Rev.* **2009**, 38, 2520-2531.
13. Winter, M.; Brodd, R. J., What are batteries, fuel cells, and supercapacitors? *Chem Rev* **2004**, 104, 4245-4269.
14. Yang, Z. G.; Zhang, J. L.; Kintner-Meyer, M. C. W.; Lu, X. C.; Choi, D. W.; Lemmon, J. P.; Liu, J., Electrochemical Energy Storage for Green Grid. *Chem Rev* **2011**, 111, 3577-3613.
15. Yu, G. H.; Xie, X.; Pan, L. J.; Bao, Z. N.; Cui, Y., Hybrid nanostructured materials for high-performance electrochemical capacitors. *Nano Energy* **2013**, 2, 213-234.
16. Pandolfo, A. G.; Hollenkamp, A. F., Carbon properties and their role in supercapacitors. *J. Power Sources* **2006**, 157, 11-27.
17. Service, R. F., Materials science - New 'supercapacitor' promises to pack more electrical punch. *Science* **2006**, 313, 902-902.
18. Brodd, R. J.; Bullock, K. R.; Leising, R. A.; Middaugh, R. L.; Miller, J. R.; Takeuchi, E., Batteries, 1977 to 2002. *J. Electrochem. Soc.* **2004**, 151, K1-K11.
19. Armand, M.; Johansson, P., Novel weakly coordinating heterocyclic anions for use in lithium batteries. *J. Power Sources* **2008**, 178, 821-825.
20. Armand, M.; Tarascon, J. M., Building better batteries. *Nature* **2008**, 451, 652-657.
21. Goodenough, J. B.; Kim, Y., Challenges for Rechargeable Li Batteries. *Chem. Mater.* **2010**, 22, 587-603.



22. Tarascon, J. M.; Armand, M., Issues and challenges facing rechargeable lithium batteries. *Nature* **2001**, 414, 359-367.
23. Burke, A. F.; Murphy, T. C., Material characteristics and the performance of electrochemical capacitors for electric/hybrid vehicle applications. *Mater Res Soc Symp P* **1995**, 393, 375-395.
24. Long, J. W.; Belanger, D.; Brousse, T.; Sugimoto, W.; Sassin, M. B.; Crosnier, O., Asymmetric electrochemical capacitors-Stretching the limits of aqueous electrolytes. *Mrs Bulletin* **2011**, 36, 513-522.
25. Gouy, G., Constitution of the electric charge at the surface of an electrolyte. *J. phys* **1910**, 9, 457-467.
26. Chapman, D. L., LI. A contribution to the theory of electrocapillarity. *The London, Edinburgh, and Dublin Philosophical Magazine and Journal of Science* **1913**, 25, 475-481.
27. Stern, O., The theory of the electrolytic double-layer. *Zeit. Elektrochem* **1924**, 30, 508-516.
28. Zhao, X.; Sanchez, B. M.; Dobson, P. J.; Grant, P. S., The role of nanomaterials in redox-based supercapacitors for next generation energy storage devices. *Nanoscale* **2011**, 3, 839-855.
29. Jiang, H.; Ma, J.; Li, C. Z., Mesoporous Carbon Incorporated Metal Oxide Nanomaterials as Supercapacitor Electrodes. *Adv. Mater.* **2012**, 24, 4197-4202.
30. Lokhande, C. D.; Dubal, D. P.; Joo, O. S., Metal oxide thin film based supercapacitors. *Curr. Appl. Phys.* **2011**, 11, 255-270.
31. Liu, C. G.; Yu, Z. N.; Neff, D.; Zhamu, A.; Jang, B. Z., Graphene-Based Supercapacitor with an Ultrahigh Energy Density. *Nano Lett.* **2010**, 10, 4863-4868.
32. Naoi, K.; Simon, P., New materials and new configurations for advanced electrochemical capacitors. *J. Electrochem. Soc* **2008**, 17, 34-37.
33. Hu, C. C.; Chang, K. H.; Lin, M. C.; Wu, Y. T., Design and tailoring of the nanotubular arrayed architecture of hydrous RuO<sub>2</sub> for next generation supercapacitors. *Nano Lett.* **2006**, 6, 2690-2695.
34. Wu, Z. S.; Wang, D. W.; Ren, W.; Zhao, J.; Zhou, G.; Li, F.; Cheng, H. M., Anchoring Hydrous RuO<sub>2</sub> on Graphene Sheets for High-Performance Electrochemical Capacitors. *Adv. Funct. Mater.* **2010**, 20, 3595-3602.
35. Chang, J. K.; Chen, Y. L.; Tsai, W. T., Effect of heat treatment on material characteristics and pseudo-capacitive properties of manganese oxide prepared by anodic deposition. *J. Power Sources* **2004**, 135, 344-353.
36. Nagarajan, N.; Humadi, H.; Zhitomirsky, I., Cathodic electrodeposition of MnOx films for electrochemical supercapacitors. *Electrochim. Acta* **2006**, 51, 3039-3045.
37. Lee, J. W.; Ahn, T.; Kim, J. H.; Ko, J. M.; Kim, J. D., Nanosheets based mesoporous NiO microspherical structures via facile and template-free method for high performance supercapacitors. *Electrochim. Acta* **2011**, 56, 4849-4857.
38. Cheng, J.; Cao, G. P.; Yang, Y. S., Characterization of sol-gel-derived NiOx xerogels as supercapacitors. *J. Power Sources* **2006**, 159, 734-741.
39. Du, X.; Wang, C. Y.; Chen, M. M.; Jiao, Y.; Wang, J., Electrochemical Performances of Nanoparticle Fe<sub>3</sub>O<sub>4</sub>/Activated Carbon Supercapacitor Using KOH Electrolyte Solution. *J Phys Chem C* **2009**, 113, 2643-2646.
40. Rudge, A.; Davey, J.; Raistrick, I.; Gottesfeld, S.; Ferraris, J. P., Conducting Polymers as Active Materials in Electrochemical Capacitors. *J. Power Sources* **1994**, 47, 89-107.
41. Fan, L. Z.; Hu, Y. S.; Maier, J.; Adelhelm, P.; Smarsly, B.; Antonietti, M., High electroactivity of polyaniline in supercapacitors by using a hierarchically porous carbon monolith as a support. *Adv. Funct. Mater.* **2007**, 17, 3083-3087.
42. Brousse, T.; Toupin, M.; Dugas, R.; Athouel, L.; Crosnier, O.; Belanger, D., Crystalline MnO<sub>2</sub> as possible alternatives to amorphous compounds in electrochemical supercapacitors. *J. Electrochem.*

Soc. **2006**, 153, A2171-A2180.

43. Zhao, X.; Zhang, L. L.; Murali, S.; Stoller, M. D.; Zhang, Q. H.; Zhu, Y. W.; Ruoff, R. S., Incorporation of Manganese Dioxide within Ultraporous Activated Graphene for High-Performance Electrochemical Capacitors. *ACS Nano* **2012**, 6, 5404-5412.
44. Chen, W.; Rakhi, R. B.; Alshareef, H. N., High energy density supercapacitors using macroporous kitchen sponges. *J. Mater. Chem.* **2012**, 22, 14394-14402.
45. Xu, C. J.; Kang, F. Y.; Li, B. H.; Du, H. D., Recent progress on manganese dioxide based supercapacitors. *J. Mater. Res.* **2010**, 25, 1421-1432.
46. Lee, H. Y.; Goodenough, J. B., Supercapacitor behavior with KCl electrolyte. *J. Solid State Chem.* **1999**, 144, 220-223.
47. Reddy, R. N.; Reddy, R. G., Sol-gel MnO<sub>2</sub> as an electrode material for electrochemical capacitors. *J. Power Sources* **2003**, 124, 330-337.
48. Long, J. W.; Young, A. L.; Rolison, D. R., Spectroelectrochemical characterization of nanostructured, mesoporous manganese oxide in aqueous electrolytes. *J. Electrochem. Soc.* **2003**, 150, A1161-A1165.
49. Moore, T.; Ellis, M.; Selwood, P., Solid Oxides and Hydroxides of Manganese<sup>1</sup>. *J. Am. Chem. Soc.* **1950**, 72, 856-866.
50. Robinson, D. M.; Go, Y. B.; Mui, M.; Gardner, G.; Zhang, Z. J.; Mastrogiovanni, D.; Garfunkel, E.; Li, J.; Greenblatt, M.; Dismukes, G. C., Photochemical Water Oxidation by Crystalline Polymorphs of Manganese Oxides: Structural Requirements for Catalysis. *J. Am. Chem. Soc.* **2013**, 135, 3494-3501.
51. Augustyn, V.; Dunn, B., Vanadium oxide aerogels: Nanostructured materials for enhanced energy storage. *C. R. Chim.* **2010**, 13, 130-141.
52. Brezesinski, K.; Wang, J.; Haetge, J.; Reitz, C.; Steinmueller, S. O.; Tolbert, S. H.; Smarsly, B. M.; Dunn, B.; Brezesinski, T., Pseudocapacitive Contributions to Charge Storage in Highly Ordered Mesoporous Group V Transition Metal Oxides with Iso-Oriented Layered Nanocrystalline Domains. *J. Am. Chem. Soc.* **2010**, 132, 6982-6990.
53. Wang, J.; Polleux, J.; Lim, J.; Dunn, B., Pseudocapacitive contributions to electrochemical energy storage in TiO<sub>2</sub> (anatase) nanoparticles. *J Phys Chem C* **2007**, 111, 14925-14931.
54. Wang, J.; Zhang, S. Q.; Guo, Y. Z.; Shen, J.; Attia, S. M.; Zhou, B.; Zheng, G. Z.; Gui, Y. S., Morphological effects on the electrical and electrochemical properties of carbon aerogels. *J. Electrochem. Soc.* **2001**, 148, D75-D77.
55. Lang, X. Y.; Hirata, A.; Fujita, T.; Chen, M. W., Nanoporous metal/oxide hybrid electrodes for electrochemical supercapacitors. *Nat. Nanotechnol.* **2011**, 6, 232-236.
56. Chen, W.; Rakhi, R. B.; Hu, L. B.; Xie, X.; Cui, Y.; Alshareef, H. N., High-Performance Nanostructured Supercapacitors on a Sponge. *Nano Lett.* **2011**, 11, 5165-5172.
57. Formas, A., US patent, 1 975 504, 1934;(b) J. Doshi and DH Reneker. *J. Electrostat* **1995**, 35, 151.
58. Greiner, A.; Wendorff, J. H., Electrospinning: A fascinating method for the preparation of ultrathin fibres. *Angew. Chem. Int. Ed.* **2007**, 46, 5670-5703.
59. Li, D.; Xia, Y. N., Direct fabrication of composite and ceramic hollow nanofibers by electrospinning. *Nano Lett.* **2004**, 4, 933-938.
60. Lee, J. S.; Kwon, O. S.; Park, S. J.; Park, E. Y.; You, S. A.; Yoon, H.; Jang, J., Fabrication of Ultrafine Metal-Oxide-Decorated Carbon Nanofibers for DMMP Sensor Application. *ACS Nano* **2011**, 5, 7992-8001.
61. Reneker, D. H.; Chun, I., Nanometre diameter fibres of polymer, produced by electrospinning. *Nanotechnology* **1996**, 7, 216.
62. Frenot, A.; Chronakis, I. S., Polymer nanofibers assembled by electrospinning. *Curr. Opin.*

*Colloid Interface Sci.* **2003**, 8, 64-75.

63. Huang, Z.-M.; Zhang, Y.-Z.; Kotaki, M.; Ramakrishna, S., A review on polymer nanofibers by electrospinning and their applications in nanocomposites. *Compos. Sci. Technol.* **2003**, 63, 2223-2253.
64. Reneker, D. H.; Yarin, A. L.; Fong, H.; Koombhongse, S., Bending instability of electrically charged liquid jets of polymer solutions in electrospinning. *J. Appl. Phys.* **2000**, 87, 4531.
65. Shin, Y.; Hohman, M.; Brenner, M.; Rutledge, G., Electrospinning: A whipping fluid jet generates submicron polymer fibers. *Appl. Phys. Lett.* **2001**, 78, 1149.
66. Yarin, A.; Koombhongse, S.; Reneker, D., Taylor cone and jetting from liquid droplets in electrospinning of nanofibers. *J. Appl. Phys.* **2001**, 90, 4836-4846.
67. Shin, Y.; Hohman, M.; Brenner, M.; Rutledge, G., Experimental characterization of electrospinning: the electrically forced jet and instabilities. *Polymer* **2001**, 42, 09955-09967.
68. Hohman, M. M.; Shin, M.; Rutledge, G.; Brenner, M. P., Electrospinning and electrically forced jets. I. Stability theory. *Phys. Fluids* **2001**, 13, 2201.
69. Hohman, M. M.; Shin, M.; Rutledge, G.; Brenner, M. P., Electrospinning and electrically forced jets. II. Applications. *Phys. Fluids* **2001**, 13, 2221.
70. Fridrikh, S. V.; Yu, J. H.; Brenner, M. P.; Rutledge, G. C., Controlling the fiber diameter during electrospinning. *Phys. Rev. Lett.* **2003**, 90.
71. Formo, E.; Yavuz, M. S.; Lee, E. P.; Lane, L.; Xia, Y. N., Functionalization of electrospun ceramic nanofibre membranes with noble-metal nanostructures for catalytic applications. *J. Mater. Chem.* **2009**, 19, 3878-3882.
72. Ding, Y.; Wang, Y.; Zhang, L. C.; Zhang, H.; Li, C. M.; Lei, Y., Preparation of TiO<sub>2</sub>-Pt hybrid nanofibers and their application for sensitive hydrazine detection. *Nanoscale* **2011**, 3, 1149-1157.
73. Zhang, M. Y.; Shao, C. L.; Guo, Z. C.; Zhang, Z. Y.; Mu, J. B.; Cao, T. P.; Liu, Y. C., Hierarchical Nanostructures of Copper(II) Phthalocyanine on Electrospun TiO<sub>2</sub> Nanofibers: Controllable Solvothermal-Fabrication and Enhanced Visible Photocatalytic Properties. *ACS Appl. Mater. Interfaces* **2011**, 3, 369-377.
74. Kim, H. M.; Chae, W. P.; Chang, K. W.; Chun, S.; Kim, S.; Jeong, Y.; Kang, I. K., Composite nanofiber mats consisting of hydroxyapatite and titania for biomedical applications. *J Biomed Mater Res B* **2010**, 94B, 380-387.
75. Cavaliere, S.; Subianto, S.; Savych, I.; Jones, D. J.; Roziere, J., Electrospinning: designed architectures for energy conversion and storage devices. *Energy Environ. Sci.* **2011**, 4, 4761-4785.
76. Li, D.; Xia, Y. N., Electrospinning of nanofibers: Reinventing the wheel? *Adv. Mater.* **2004**, 16, 1151-1170.
77. Reneker, D. H.; Hou, H. Q.; Rangkupan, R.; Lennhoff, J. D., Electrospinning polymer nanofibers in a vacuum. *Abstr Pap Am Chem S* **2003**, 226, U425-U425.
78. Koombhongse, S.; Liu, W. X.; Reneker, D. H., Flat polymer ribbons and other shapes by electrospinning. *J. Polym. Sci. Part B-Polym. Phys.* **2001**, 39, 2598-2606.
79. Fong, H.; Liu, W. D.; Wang, C. S.; Vaia, R. A., Generation of electrospun fibers of nylon 6 and nylon 6-montmorillonite nanocomposite. *Polymer* **2002**, 43, 775-780.
80. Krishnappa, R. V. N.; Desai, K.; Sung, C. M., Morphological study of electrospun polycarbonates as a function of the solvent and processing voltage. *J. Mater. Sci.* **2003**, 38, 2357-2365.
81. Sun, Z. C.; Zussman, E.; Yarin, A. L.; Wendorff, J. H.; Greiner, A., Compound core-shell polymer nanofibers by co-electrospinning. *Adv. Mater.* **2003**, 15, 1929-+.
82. Bognitzki, M.; Frese, T.; Steinhart, M.; Greiner, A.; Wendorff, J. H.; Schaper, A.; Hellwig, M., Preparation of fibers with nanoscaled morphologies: Electrospinning of polymer blends. *Polym. Eng. Sci.* **2001**, 41, 982-989.

83. Dai, H. Q.; Gong, J.; Kim, H.; Lee, D., A novel method for preparing ultra-fine alumina-borate oxide fibres via an electrospinning technique. *Nanotechnology* **2002**, 13, 674-677.
84. Viswanathamurthi, P.; Bhattarai, N.; Kim, H. Y.; Lee, D. R.; Kim, S. R.; Morris, M. A., Preparation and morphology of niobium oxide fibres by electrospinning. *Chem. Phys. Lett.* **2003**, 374, 79-84.
85. Shao, C. L.; Kim, H. Y.; Gong, J.; Ding, B.; Lee, D. R.; Park, S. J., Fiber mats of poly(vinyl alcohol)/silica composite via electrospinning. *Mater. Lett.* **2003**, 57, 1579-1584.
86. Dharmaraj, N.; Park, H. C.; Lee, B. M.; Viswanathamurthi, P.; Kim, H. Y.; Lee, D. R., Preparation and morphology of magnesium titanate nanofibres via electrospinning. *Inorg. Chem. Commun.* **2004**, 7, 431-433.
87. Kim, C.; Yang, K. S., Electrochemical properties of carbon nanofiber web as an electrode for supercapacitor prepared by electrospinning. *Appl. Phys. Lett.* **2003**, 83, 1216-1218.
88. Hou, H. Q.; Reneker, D. H., Carbon nanotubes on carbon nanofibers: A novel structure based on electrospun polymer nanofibers. *Adv. Mater.* **2004**, 16, 69-+.
89. Kim, C.; Ngoc, B. T. N.; Yang, K. S.; Kojima, M.; Kim, Y. A.; Kim, Y. J.; Endo, M.; Yang, S. C., Self-sustained thin webs consisting of porous carbon nanofibers for supercapacitors via the electrospinning of polyacrylonitrile solutions containing zinc chloride. *Adv. Mater.* **2007**, 19, 2341-+.
90. Jänes, A.; Tönurist, K.; Thomberg, T.; Lust, E., Comparison of Electrospun and Commercially Available Separator Materials for Supercapacitors. *ECS Trans.* **2009**, 19, 23-32.
91. Park, S. J.; Im, S. H., Electrochemical behaviors of PAN/Ag-based carbon nanofibers by electrospinning. *Bull. Korean Chem. Soc.* **2008**, 29, 777-781.
92. Li, J.; Liu, E.-h.; Li, W.; Meng, X.-y.; Tan, S.-t., Nickel/carbon nanofibers composite electrodes as supercapacitors prepared by electrospinning. *J. Alloys Compd.* **2009**, 478, 371-374.
93. Guo, Q. H.; Zhou, X. P.; Li, X. Y.; Chen, S. L.; Seema, A.; Greiner, A.; Hou, H. Q., Supercapacitors based on hybrid carbon nanofibers containing multiwalled carbon nanotubes. *J. Mater. Chem.* **2009**, 19, 2810-2816.
94. Ahn, Y. R.; Park, C. R.; Jo, S. M.; Kim, D. Y., Enhanced charge-discharge characteristics of RuO<sub>2</sub> supercapacitors on heat-treated TiO<sub>2</sub> nanorods. *Appl. Phys. Lett.* **2007**, 90.
95. Hyun, T. S.; Tuller, H. L.; Youn, D. Y.; Kim, H. G.; Kim, I. D., Facile synthesis and electrochemical properties of RuO<sub>2</sub> nanofibers with ionically conducting hydrous layer. *J. Mater. Chem.* **2010**, 20, 9172-9179.
96. Lin, C. K.; Chuang, K. H.; Lin, C. Y.; Tsay, C. Y.; Chen, C. Y., Manganese oxide films prepared by sol-gel process for supercapacitor application. *Surf. Coat. Technol.* **2007**, 202, 1272-1276.
97. Logothetis, E. M.; Park, K., Electrical-Conductivity of Mn<sub>3</sub>O<sub>4</sub>. *Solid State Commun.* **1975**, 16, 909-912.
98. Klose, P. H., ELECTRICAL PROPERTIES OF MANGANESE DIOXIDE AND MANGANESE SESQUIOXIDE. *J. Electrochem. Soc.* **1970**, 117, 854-&.
99. Nathan, T.; Cloke, M.; Prabakaran, S. R. S., Electrode Properties of Mn<sub>2</sub>O<sub>3</sub> Nanospheres Synthesized by Combined Sonochemical/Solvothermal Method for Use in Electrochemical Capacitors. *J. Nanometer.* **2008**.
100. Song, M. K.; Cheng, S.; Chen, H. Y.; Qin, W. T.; Nam, K. W.; Xu, S. C.; Yang, X. Q.; Bongiorno, A.; Lee, J.; Bai, J. M.; Tyson, T. A.; Cho, J.; Liu, M. L., Anomalous Pseudocapacitive Behavior of a Nanostructured, Mixed-Valent Manganese Oxide Film for Electrical Energy Storage. *Nano Lett.* **2012**, 12, 3483-3490.